$k_\perp$-factorization and forward jets

Sergey Baranov, Jochen Bartels, Michal Deák, Francesco Hautmann, Hannes Jung,
Albert Knutsson, Krzysztof Kutak, Artem Lipatov, Christophe Royon, Augustín Sabio Vera,
Florian Schwennsen, Nikolai Zotov

Hadronic final states containing multiple jets have been investigated at the Tevatron and HERA colliders, and will play a central role in the Large Hadron Collider (LHC) physics program. The interpretation of experimental data for such final states relies both on perturbative multi-jet calculations (see [1] for a recent overview) and on realistic event simulation by parton-shower Monte Carlo generators (see e.g. [2–6]).

Owing to the complex kinematics involving multiple hard scales and the large phase space opening up at very high energies, multi-jet events are potentially sensitive to effects of QCD initial-state radiation that depend on the finite transverse-momentum tail of partonic matrix elements and distributions.

Standard shower Monte Carlos reconstructing exclusive events, such as HERWIG [7,8] and PYTHIA [9], are based on collinear evolution of the initial-state jet. Finite-$k_\perp$ contributions are not included, but rather correspond to corrections [10–14] to the angular or transverse-momentum ordering implemented in the parton-branching algorithms. The theoretical framework to take these corrections into account is based on using initial-state distributions unintegrated in both longitudinal and transverse momenta [12–14], coupled to hard matrix elements (ME) suitably defined off mass shell. See e.g. [15] for discussion of the Monte Carlo shower implementation of the method. Event generators based on $k_\perp$-dependent showers of this kind include [16–22].

We give a short introduction to $k_\perp$-factorization and describe the determination of unintegrated parton density functions (uPDFs). Then we discuss the calculation of new processes in the frame of $k_\perp$-factorisation and show a comparison with measurements at the Tevatron. A summary of NLO calculations for multi-jet production in ep and pp in $k_\perp$-factorisation follows. Finally, we discuss forward jet production and the azimuthal decorrelation of jets both in ep and pp, signatures which could clearly show evidence for small x parton dynamics.

1   Short introduction to $k_\perp$-factorization and uPDFs

Author: Francesco Hautmann, Hannes Jung

In $k_\perp$-factorization the cross section for any process $pp \to X$ can be written as:

$$\sigma = \int dx_1 dx_2 \int dk_{\perp 1} dk_{\perp 2} \mathcal{A}(x_1, k_{\perp 1}, q) \mathcal{A}(x_2, k_{\perp 2}, q) \hat{\sigma}(x_1, x_2, k_{\perp 1}, k_{\perp 2}, q) \tag{1}$$

with $\mathcal{A}(x, k_\perp, q)$ being the un-integrated transverse momentum ($k_\perp$- dependent) parton density function (uPDF or TMD), q defines the factorization scale and $\hat{\sigma}$ is the partonic cross section taken with off-shell initial partons. Here we concentrate on the small x region, which is described by high-energy factorization (or $k_\perp$-factorisation).

Both the uPDF and the off-shell partonic cross section can be formulated in the small x region where a gauge-invariant definition emerges from high-energy factorization [12–14]. It has

been used for studies of collider processes both by Monte Carlo (see reviews in [23–25]) and by semi-analytic resummation approaches (see [26, 27]).

To characterize a transverse momentum dependent parton distribution gauge-invariantly over the whole phase space is a nontrivial question [28, 29], currently at the center of much activity. See overview in [24].

The diagrammatic argument for gauge invariance, given in [12–14], and developed in [30, 31], is based on relating off-shell matrix elements with physical cross sections at $x \ll 1$, and exploits the dominance of single gluon polarization at high energies.[1] The main reason why a natural definition for TMD pdfs can be constructed in the high-energy limit is that one can relate directly (up to perturbative corrections) the cross section for a *physical* process, say, photoproduction of a heavy-quark pair, to an *unintegrated* gluon distribution, much as, in the conventional parton picture, one does for DIS in terms of ordinary (integrated) parton distributions. On the other hand, the difficulties in defining a TMD distribution over the whole phase space can largely be associated with the fact that it is not obvious how to determine such a relation for general kinematics.

The evolution equations obeyed by TMD distributions defined from the high-energy limit are of the type of energy evolution [32]. Factorization formulas in terms of TMD distributions [12–14] have corrections that are down by logarithms of energy rather than powers of momentum transfer. On the other hand, it is important to observe that this framework allows one to describe the ultraviolet region of arbitrarily high $k_\perp$ and in particular re-obtain the structure of QCD logarithmic scaling violations [26, 27, 30, 31]. This ultimately justifies the use of this approach for jet physics. In particular it is the basis for using corresponding Monte Carlo implementations [15–22] to treat multi-scale hard processes at the LHC.

From both theoretical and phenomenological view-points, it is one of the appealing features of the high-energy framework for TMD distributions that one can relate its results to a well-defined summation of higher-order radiative corrections. By expanding these results to fixed order in α_s, one can match the predictions thus obtained against perturbative calculations. This has been verified for a number of specific processes at next-to-leading order (see for instance [33–35] for heavy flavor production) and more recently at next-to-next-to-leading order (see for instance [36, 37]). Note that this fact also provides the basis for shower algorithms implementing this framework to be combined with fixed-order NLO calculations by using existing techniques for such matching.

2   Prospects and recent developments of $k_\perp$-factorization

At HERA the $k_\perp$- factorization approach has been successfully applied to describe multi-jet production as well as the production of heavy quarks at small values of x, which are dominated by gluon initiated processes. The relevant off-shell matrix elements for jet and heavy quark production are known since long. The unintegrated gluon distribution has been determined using inclusive measurements at HERA. A new determination of the uPDF using also final state measurements is described in section 2.1.

---

[1]It is emphasized e.g. in [23, 29] that a fully worked out operator argument, on the other hand, is highly desirable but is still missing.

However to apply $k_\perp$- factorization to describe measurements in general in $p\bar{p}$ or pp new and additional matrix elements for different processes need to be calculated. In the following, the calculation of new processes will be presented:

- $g^*q \rightarrow gq$ to describe jet production in the forward and backward region
- $g^*g^* \rightarrow \gamma/W/Z + q\bar{q}$ to describe the inclusive production of $\gamma/W/Z$
- $g^*q \rightarrow \gamma q$ to describe prompt photon production

Since some of the processes are quark initiated, unintegrated quark densities need to be determined. In a simplest approach we allow only valence quarks (at large x). The contribution of quark initiated processes is discussed in section 2.3 explicitly.

The aim of this contribution is to show the two areas, where improvements in the $k_\perp$-factorization approach has been made: the determination of the uPDFs and the calculation of matrix elements.

2.1 An approach to fast fits of the unintegrated gluon density

Author: Alessandro Bacchetta, Albert Knutsson, Krzysztof Kutak

In perturbative QCD the PDFs are given by solutions of integral equations, for which the initial input distributions have to be determined by fits to experimental data. It turns out that, in general it is not efficient to tune Monte Carlo event generators (MC) by sequential calls of the generator together with a minimisation program. Motivated by [38], we use an alternative fitting method, which is based on producing a grid in parameter-observable space. This allows the parameter dependence to be determined by polynomial interpolation before the fit is performed, which significantly reduces the time to do the fit itself.

Here we determine the parameters in the starting distribution of the unintegrated gluon density function by fits to deep inelastic scattering F_2 structure function data from the H1 experiment [39]. This is carried out by using the CASCADE Monte Carlo event generator [16].

The Unintegrated Gluon Density

The starting distribution of the unintegrated gluon density is parameterized as

$$A_0(x, k_t) = Nx^{-B}(1-x)^C(1-Dx)\exp\left[(k_t - \mu)^2/\sigma^2\right]$$

where x is the longitudinal momentum fraction of the proton carried by the gluon and k_t its transverse momentum. In this study the N (normalisation), B (low x behaviour), D are determined. The parameters C, σ and μ, are kept fixed at $C = 4$, $\sigma = 1$ and $\mu = 0$.

The unintegrated gluon density is determined by a convolution of the non-perturbative starting distribution $\mathcal{A}_0(x)$ and the CCFM evolution denoted by $\tilde{\mathcal{A}}(x, k_\perp, \bar{q})$:

$$x\mathcal{A}(x, k_\perp, \bar{q}) = \int dx' \mathcal{A}_0(x', k_\perp) \cdot \frac{x}{x'}\tilde{\mathcal{A}}\left(\frac{x}{x'}, k_\perp, \bar{q}\right)$$

The Fitting Method

In the first step of the fitting procedure we build up a grid of MC predictions in the parameter space $(p_1, p_2, \ldots, p_n)$ for each of the observables X. Then we use the grid to describe the parameter space analytically by a polynomial of the form

$$X(p_1, p_2, .., p_n) = A_0 + \sum_{i=1}^{n} B_i p_i + \sum_{i=1}^{n} C_i p_i^2 + \sum_{i=1}^{n-1} \sum_{j=i+i}^{n} D_{ij} p_i p_j + \text{H.O.}$$

We determine the coefficients A_0, B_1,... by singular value decomposition (SVD) [40], since they form an over determined system of linear equations. This is done separately for each of the MC predicted observables, which in our case corresponds to 58 experimental data points.

In order to account for correlations between parameters the form of the polynomial has to be of order higher than one. In the presented fit we use a forth order polynomial, which gives a good description of the parameter space. The $\chi^2/n.d.f.$, averaged over the 58 MC predicted observables, is $\chi^2/n.d.f = 501.7/(440-35) = 1.2$, where 440 is the number of MC grid points and 35 is the number of coefficients in the polynomial of the fourth degree.

Having described with the polynomials the behavior of the MC predictions in parameter space, we can find the values of the parameters p_1, p_2, ... for which the MC best reproduces the measurements. This is done by applying a χ^2 minimisation to

$$\chi^2 = \sum_k \frac{(X_{k,poly} - X_{k,data})^2}{\delta X_{k,poly}^2 + \delta X_{k,data}^2}$$

where the sum runs over all bins, k. $X_{k,data}$ is the measured data, with the corresponding experimental error $\delta X_{k,data}$, and $X_{k,poly}$ the polynomial prediction, with the error $\delta X_{k,poly}$ calculated from the individual errors of the fitted coefficients by using the covariance matrix. To perform this last step we use MINUIT [41], since the dependence on the parameters $p_1, p_2, ...$ is non-linear.

The method turns out to be very time-efficient, in particular since the MC grid points are generated simultaneously.

Results

The unintegrated PDF has been fitted to the proton structure function, F_2, in the kinematical range $Q^2 > 4.5$ GeV^2 and $x_{Bj} < 0.005$, where Q^2 is the virtuality of the exchanged boson and x_{Bj} is the Bjorken scaling variable. In Fig. 1 the result of the fit is compared to the data [39]. The parameter values determined from the new fit are $N = 0.221 \pm 0.011$, $B = 0.201 \pm 0.007$ and $D = -24.6 \pm 1.5$. χ^2 profiles for these parameters are shown in Fig. 2 and confirm that this is a minimum for N, B and D. Confidence regions for these parameters are shown in Fig. 3.

The χ^2/ndf of the new fit is 2.4 which is more than one unit better than obtained when using CASCADE together with the PDF set A0 [16]. The constraints on the parameters of the gluon could be hopefully further improved by fitting the k_t-dependent part of the gluon distribution. In Fig. 4 the new gluon distribution and set A0 are drawn as a function of x for two different values of k_t^2.
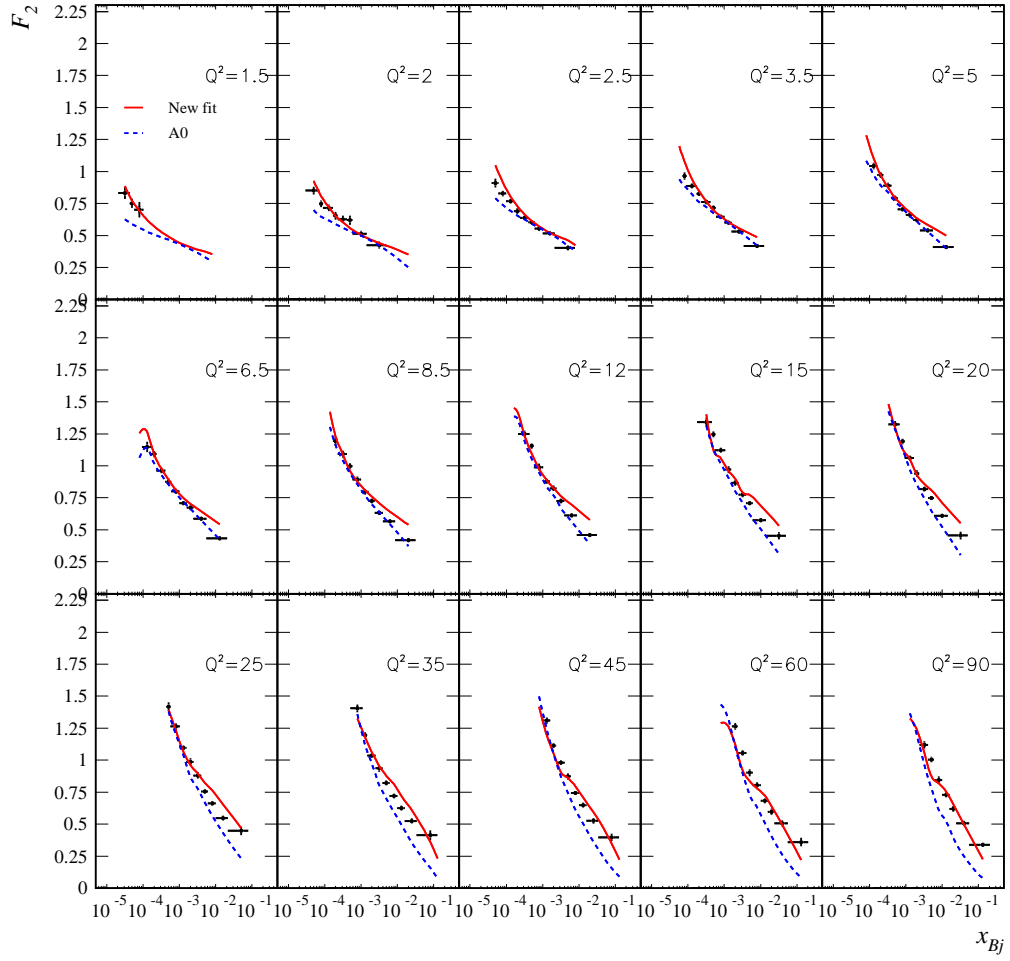
Fig. 1: *F_2 structure function data, as a function of x_{Bj} in Q^2 bins compared to predictions from the* CASCADE *Monte Carlo event generator using the newly fitted PDF (continuous red line) and old PDF set A0 (blue dashed line).The new fitted PDF has been determined in the kinematic range $Q^2 > 4.5$ GeV^2 and $x_{Bj} < 0.005$*

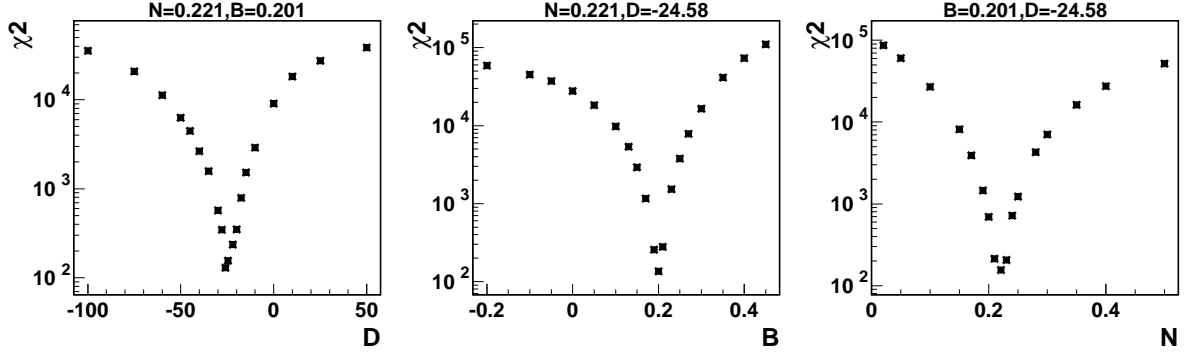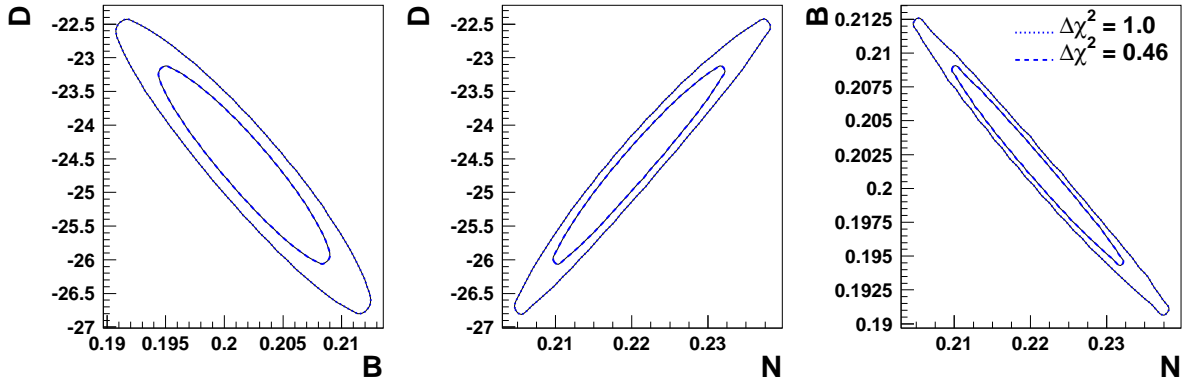Fig. 2: *χ^2 as a function of the fitted parameters.*

Fig. 3: *Confidence regions for N, B and D*

2.2 Hard matrix element calculation

For jet production at high energies the following processes contribute: $gg \rightarrow q\bar{q}$, $gg \rightarrow gg$, $qg \rightarrow qg$, $qq \rightarrow qq$ and $q\bar{q} \rightarrow q\bar{q}$. In collinear factorization (with on-shell initial partons) these processes are calculated in LO ($\mathcal{O}(\alpha_s)$) and also higher order corrections are known. In $k_\perp$- factorization the process $gg \rightarrow q\bar{q}$ are known [13, 42]. At high energies, gluon induced processes are expected to dominate. The process $g^* g^* \rightarrow gg$ is not yet considered, as there will be contributions of similar type from the parton branching. However, if jet production in the forward or backward region is considered, scattering a small x gluon off a large x valence quark ($qg^* \rightarrow qg$) will contribute significantly. This process will be described below.

The production of Z/W is calculated to a high precision in collinear factorization, even to NNLO. However, significant effects from small x partons, which are not included in the collinear treatment could become important, as suggested by [43]. Since W/Z production is the standard candle at LHC, it is important to understand in detail any possible small x effect. The Z/W production has been calculated for the first time in the framework of $k_\perp$- factorization in [44, 45] for the lowest order gluon induced process $g^* g^* \rightarrow Z/W + Q_i \bar{Q}_j$. In [45] attempts are made to include also quark initiated processes to Z/W production.
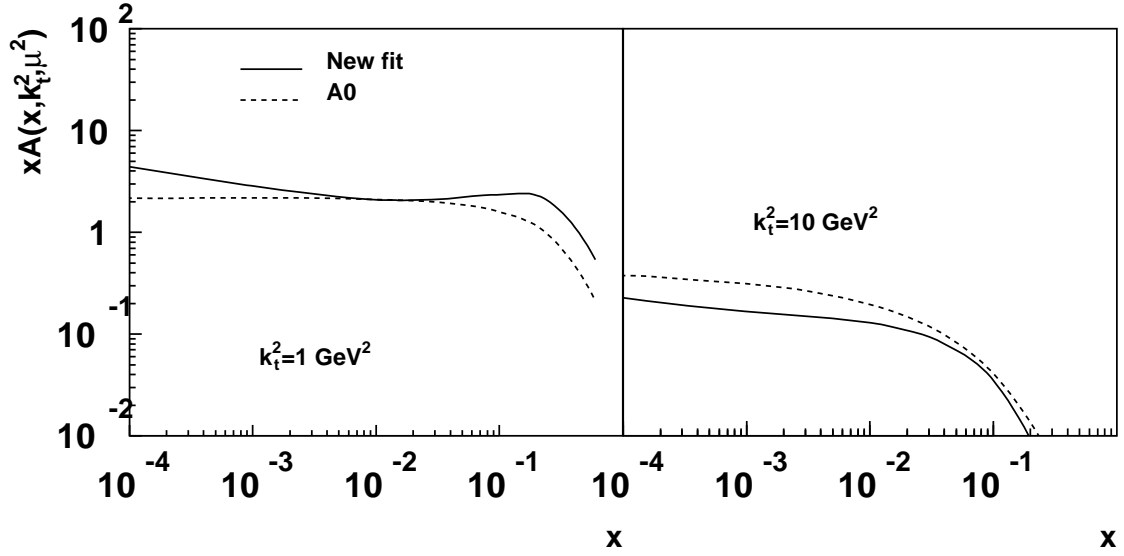
Fig. 4: *The newly fitted PDF (continuous line) compared to the old PDF set A0 (dashed line), drawn as a function of x for $k_t^2 = 1\,GeV^2$ and $k_t^2 = 10\,GeV^2$ at a scale $\mu^2 = 4\,GeV^2$.*

Process $qg^* \rightarrow qg$ at the LHC

Author: Michal Deak, Krzysztof Kutak

Here we consider a very asymmetric situation in proton proton scattering in which an off-shell gluon coming from one of the protons scatters off an on-shell valence quark from the other proton. We can use small x dynamics for the gluon where the $k_\perp$-factorization formalism is justified and on the other side we use collinear large x dynamics for the valence quark. The matrix element of the hard subprocess is factorized from the unintegrated gluon density function by $k_\perp$- factorization theorem and from the valence quark uPDF.

Similar to the $Z/W + Q_i\bar{Q}_j$ case ([44] and [45]), we will use Sudakov decomposition for the four-momenta of the initial state and final state particles.

$$k = x_g p_A + z_g p_B + k_\perp \tag{2}$$

$$q = x_q p_B \tag{3}$$

$$k' = x'_g p_A + z'_g p_B + k'_\perp \tag{4}$$

$$q' = z'_q p_A + x'_q p_B + q'_\perp \tag{5}$$

$$t = (k - k')^2 \tag{6}$$

The amplitude for the process $g^*q \rightarrow gq$ consists of the diagrams in Fig. 5. The squared matrix element, after summing over colors of final and initial state particles, is calculated using the $k_\perp$- factorization prescription:

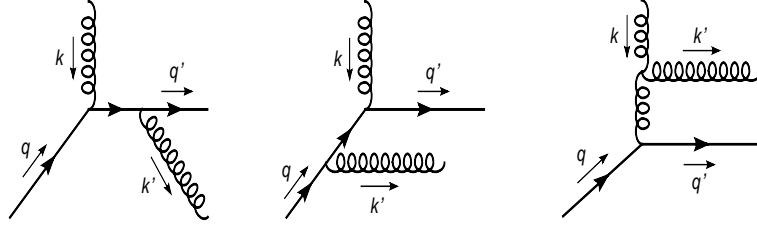$$|\mathcal{M}|^2 = \frac{1}{4} \frac{1}{N_c(N_c^2 - 1)} \left(C_A C_F^2 A_{abelian} + C_A^2 C_F A_{nonabelian} \right) \tag{7}$$

Fig. 5: Full set of diagrams of $qg^* \to qg$ with initial state gluon off-shell required by gauge invariance. a) Diagrams similar to diagrams in collinear factorization approaach, b) additional diagrams required by gauge invariance.

where

$$A_{abelian} = (4\pi\alpha_s)^2 \left(\frac{k \cdot q}{p \cdot q}\right)^2 \frac{(p \cdot q)^2 + (p \cdot q')^2}{k' \cdot q \; k' \cdot q'} \tag{8}$$

and

$$A_{nonabelian} = (4\pi\alpha_s)^2 \left(\frac{k \cdot q}{p \cdot q}\right)^2 \frac{(p \cdot q)^2 + (p \cdot q')^2}{2 k' \cdot q \; k' \cdot q'} \left(\frac{2k' \cdot q' \; p \cdot q}{-t \, k' \cdot p} + \frac{2k' \cdot q \; p \cdot q'}{-t \, k' \cdot p} - 1\right) \tag{9}$$

with $C_A = N_c$, $C_F = (N_c^2 - 1)/(2N_c)$ and N_c being the number of colours. The $k_\perp \to 0$ can be performed and the text book result for $qg \to qg$ is recovered.

The matrix element is singular when one of the particles in final state is collinear with the quark in initial state. To regularize the matrix element we set a cut on the transverse momenta of each of final state particles in the laboaratory frame, $|\mathbf{k}'| > p_{\perp cut}$ and $|\mathbf{q}'| > p_{\perp cut}$. We note that a cut on one of the transverse momenta is not enough to avoid divergencies.

Z and W production associated with heavy quark-antiquark pair

The calculation of the matrix element for the process $g^*g^* \to Z/W + Q_i\bar{Q}_j$ is described in detail in [44,45]. The calculations differ in the way the spin density of the initial state is treated. However, they are equivalent and give the same results for the matrix element of the hard subprocess. We have cross-checked the calculations numerically and found agreement of the cross sections at Tevatron and LHC energies at the 0.1 % level.

2.3 Implications for the LHC: Electroweak gauge boson production in hadronic collisions at high energies

Author: Serguei Baranov, Artem Lipatov, Nikolai Zotov

AT HERA and the Tevatron $k_\perp$- factorization supplemented with the BFKL-like gluon dynamics was successfully applied to describe various measurements of heavy quark production [46, 47] (and references therein). It is important that these predictions were based on the off-shell matrix elements $\gamma g^* \to Q\bar{Q}$ or $g^*g^* \to Q\bar{Q}$. In Ref. [48,49] inclusive Higgs hadroproduction at Tevatron and LHC energies has been investigated, where the main contribution also

came from the off-shell gluon-gluon fusion. It was demonstrated that using the CCFM-evolved unintegrated gluon densities results in predictions which are very close to the NNLO pQCD ones. This encouraged us to apply the $k_\perp$- factorization approach also to the production of inclusive electroweak gauge bosons.

At leading order (LO) QCD, the $W^\pm$ and Z^0 bosons are produced via quark-antiquark annihilation $q + \bar{q}' \to W/Z$. Here, an important component of the calculations are the unintegrated quark distributions. At present, these distributions are only available in the Kimber-Martin-Ryskin (KMR) scheme [50, 51], since there are theoretical difficulties in obtaining quark distributions directly from CCFM and BFKL equations. This is in contrast to gluon-induced processes where many unintegrated gluon densities are available.

Since sea quarks can appear as a result of gluon splitting, at the price of absorbing the last gluon splitting into the hard subprocess (i.e., considering the $2 \to 2$ and $2 \to 3$ rather than $2 \to 1$ matrix elements), the problem of poorly known sea quark densities can efficiently be reduced to the problem of gluon densities. However, it is not evident in advance whether the last gluon splitting dominates. This issue is addressed in Ref. [45, 52]. One of the goals of that study is to clarify, to what extent the quark contributions can be reexpressed in terms of the gluon contributions. At the same time, by considerng the higher order matrix elements we take into account the terms not containing large logarithms, i.e., the terms not included in the evolution equations. Within our scheme, we get a numerical estimate of the corresponding contributions.

Our theoretical approach is the following. We start from the leading order $\mathcal{O}(\alpha)$ subprocess $q + \bar{q}' \to W/Z$, and then divide it into several contributions which correspond to the interactions of valence quarks $q_v(x, \mathbf{k}_T^2, \mu^2)$, sea quarks appearing at the last step of the gluon evolution $q_g(x, \mathbf{k}_T^2, \mu^2)$, and sea quarks coming from the earlier steps $q_s(x, \mathbf{k}_T^2, \mu^2)$. Here we use the specific property of the KMR scheme which enables us to discriminate between the various components of the quark densities.

The KMR approach represents an approximate treatment of the parton evolution mainly based on the DGLAP equation and incorporating BFKL effects at the last step of the parton ladder only, in the form of properly defined Sudakov formfactors $T_q(\mathbf{k}_T^2, \mu^2)$ and $T_g(\mathbf{k}_T^2, \mu^2)$. These formfactors already include logarithmic loop correction. Also, there are nonlogarithmic corrections which result in a K-factor on the cross section given by [53] $K(q + \bar{q}' \to W/Z) \simeq \exp\left[C_F \pi \alpha_s(\mu^2)/2\right]$ with $C_F = 4/3$ and $\mu^2 = \mathbf{p}_T^{4/3} m^{2/3}$. In this approximation, the unintegrated quark and gluon distributions are expressed by

$$f_q(x, \mathbf{k}_T^2, \mu^2) = T_q(\mathbf{k}_T^2, \mu^2) \frac{\alpha_s(\mathbf{k}_T^2)}{2\pi} \times$$
$$\times \int\limits_x^1 dz \left[P_{qq}(z) \frac{x}{z} q\left(\frac{x}{z}, \mathbf{k}_T^2\right) \Theta\left(\Delta - z\right) + P_{qg}(z) \frac{x}{z} g\left(\frac{x}{z}, \mathbf{k}_T^2\right) \right], \tag{10}$$

$$f_g(x, \mathbf{k}_T^2, \mu^2) = T_g(\mathbf{k}_T^2, \mu^2) \frac{\alpha_s(\mathbf{k}_T^2)}{2\pi} \times$$
$$\times \int\limits_x^1 dz \left[\sum_q P_{gq}(z) \frac{x}{z} q\left(\frac{x}{z}, \mathbf{k}_T^2\right) + P_{gg}(z) \frac{x}{z} g\left(\frac{x}{z}, \mathbf{k}_T^2\right) \Theta\left(\Delta - z\right) \right], \tag{11}$$
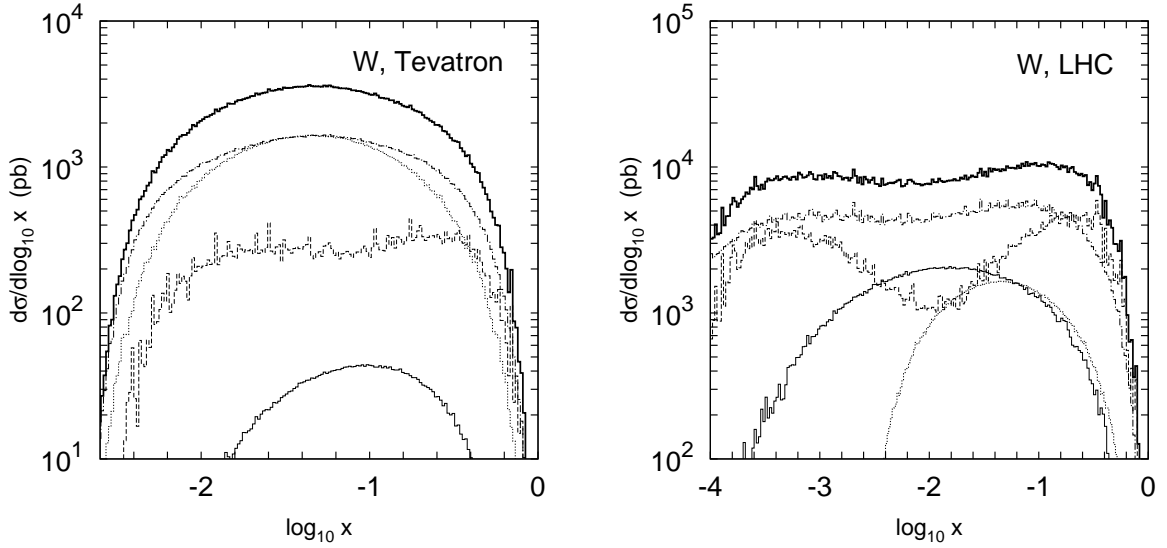
Fig. 6: Different contributions to the inclusive $W^\pm$ boson production at the Tevatron (left panel) and LHC (right panel) conditions. The solid, dashed and dotted histograms represent the contributions from the $g^* + g^* \to W^\pm/Z^0 + q + \bar{q}'$, $q_v + g^* \to W^\pm/Z^0 + q'$ and $q_v + \bar{q}'_v \to W^\pm/Z^0$ subprocesses, respectively. The dash-dotted histograms represent the "reduced sea" component. The thick solid histograms represent the sum of all contributions.

where $P_{ab}(z)$ are the usual unregularised leading order DGLAP splitting functions, and $q(x, \mu^2)$ and $g(x, \mu^2)$ are the conventional (collinear) quark and gluon densities. The function $f_q(x, \mathbf{k}_T^2, \mu^2)$ in Eq. (10) represents the total quark distribution. Modifying Eq. (10) in such a way that only the first term is kept and the second term omitted, we switch the last gluon splitting off, thus excluding the $q_g(x, \mathbf{k}_T^2, \mu^2)$ component. Taking the difference between the quark and antiquark densities we extract the valence quark component $q_v(x, \mathbf{k}_T^2, \mu^2) = f_q(x, \mathbf{k}_T^2, \mu^2) - f_{\bar{q}}(x, \mathbf{k}_T^2, \mu^2)$.

Summing up, we consider the following partonic subprocesses: gluon-gluon fusion $g + g \to W/Z + q + \bar{q}'$, with which the $q_g + \bar{q}_g$ annihilation is replaced; valence and sea quark-gluon scattering $q_v + g \to W/Z + q$ and $q_s + g \to W/Z + q$, with which the $q_v + \bar{q}_g$ and $q_s + \bar{q}_g$ annihilation is replaced; and quark-antiquark annihilation $q + \bar{q}' \to W/Z$ including both valence q_v and sea q_s quark components. The calculation of the matrix elements is explained in section 2.2. The basic formulas for coresponding contributions to the cross section are given in [45, 52].

Now we turn to numerical results. The solid, dashed and dotted histograms in fig. 2.3 represent the contributions from the $g^* + g^* \to \gamma/W^\pm/Z^0 + q + \bar{q}'$, $q_v + g^* \to \gamma/W^\pm/Z^0 + q'$ and $q_v + \bar{q}'_v \to W^\pm/Z^0$ (or $q_v + \bar{q}_v \to \gamma + g$) subprocesses, respectively. The dash-dotted histograms represent the sum of the contributions from the $q_s + \bar{q}'_s \to W^\pm/Z^0$, $q_s + g^* \to \gamma/W^\pm/Z^0 + q'$ and $q_v + \bar{q}'_s \to W^\pm/Z^0$ (or $q_s + \bar{q}_s \to \gamma + g$ and $q_v + \bar{q}_s \to \gamma + g$) subprocesses. We find that the contribution from the valence quark-antiquark annihilation is important at the Tevatron but yields only about few percent at the LHC energy. The gluon-gluon fusion is unimportant at the
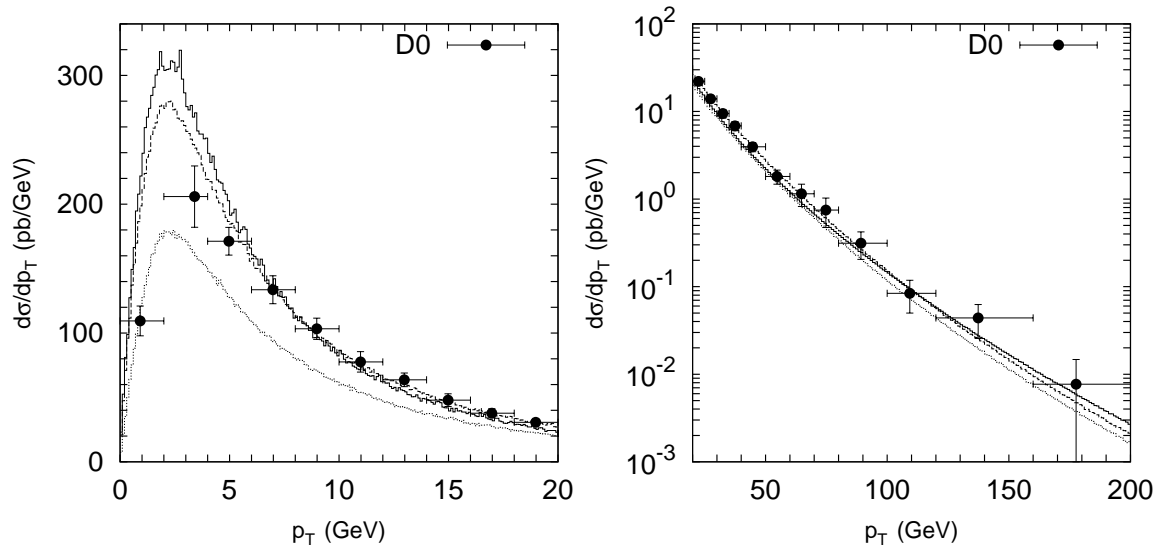
Fig. 7: Transverse mometum distribution of the $W^{\pm}$ boson production calculated at $\sqrt{s} = 1800$ GeV. Solid histograms represent calculations in the "decomposition" scheme where all contributions described in the text are taken into account. Dashed histograms correspond to the predictions based on the simple $2 \rightarrow 1$ quark-antiquark annihilation subprocess with all quark components summed together. Dotted histograms correspond to the simple $2 \rightarrow 1$ quark-antiquark annihilation subprocess without K-factor. The cross sections times branching fraction $f(W \rightarrow l\nu)$ are shown. The experimental data are from D0.
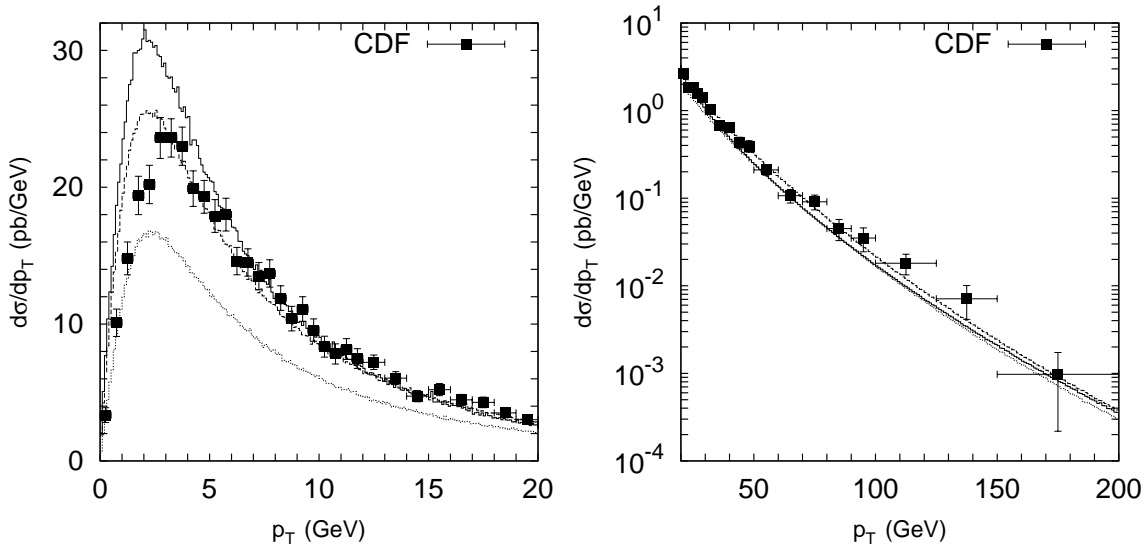
Fig. 8: Transverse mometum distribution of the Z^0 boson. Notation of the histograms is as in Fig.2.3. The experimental data are from CDF.

Tevatron, but becomes important at higher energies and has to be taken into account at the LHC. Quite a significant fraction (nearly 50%) of the calculated cross section at both the Tevatron and the LHC conditions comes from the q_s quark component. The gluon-gluon fusion contributes about $\sim 1\%$ to the total cross section at Tevatron and up to $\sim 25\%$ at the LHC.

Figs. 2.3 and 2.3 display a comparison between the calculated differential cross sections $d\sigma/dp_T$ and the experimental data [54–56] at low p_T ($p_T < 20$ GeV), and in the full p_T range. For comparison, we also show the predictions based on the simple $2 \rightarrow 1$ quark-antiquark annihilation subprocess (dotted histograms), with all quark components summed together. The difference between the results can probably be attributed to the terms not containing large logarithms. The predictions of the "subprocess decomposition" scheme lie by about a factor of 1.25 higher and show better agreement with the data.

Having considered the different partonic subprocesses we see that the dominant contribution comes from the sea quark interactions $q_s + q_s \rightarrow W/Z$, $q_s + q_v \rightarrow W/Z$ and $q_s + g \rightarrow W/Z + q'$. Notably, we find that these subprocesses are mainly due to the quarks emerging from the earler steps of the parton evolution rather than from the last gluon splitting. Thus, we conclude that the quarks constitute an important component of the parton ladder, not negligible even at the LHC energies and not reducible to the gluon component. Quarks need to be directly included in the evolution equations for consistency and completeness of the latter.

The results of our calculations within the "subprocess decomposition" scheme reasonably agree with the available experimental data and show no need for an extra factor introduced in [57].

2.4 Implications for the LHC: Z and W associated with heavy quark pair at Tevatron and the LHC in $k_\perp$-factorization

Author: Michal Deak, Florian Schwennsen

To calculate the cross section for $pp \to Z/W + Q_i \bar{Q}_j$ with the hard subprocess $g^* g^* \to Z/W + Q_i \bar{Q}_j$ at LHC energies we have to convolute the corresponding partonic off-shell cross section with gluon uPDFs. For this purpose we implemented the matrix element squared of the subprocess $g^* g^* \to Z/W + Q_i \bar{Q}_j$ into the Monte Carlo generator CASCADE.

Our calculation of the hard matrix elements includes $W^\pm$ and Z production in association with all possible quark-antiquark channels in gluon gluon fusion. Since the basic structure of all these matrix elements is very similar, we present results only for the typical case of $Zb\bar{b}$ production at LHC energies of $\sqrt{s} = 14$TeV. We compare our calculation with a prediction using collinear factorization as obtained from the program MCFM [58]. For the collinear factorization calculations we use the parton densities CTEQ6L1 [59]. Since we want compare with NLO collinear calculation, which in MCFM is available only in massless quark approximation, we compare by setting the quark mass to zero in our mass dependent calculation. To emulate the quark mass effect we set a cutoff on the transversal momenta of the quarks with values $p_{b\perp min} = m_b = 4.62$ GeV in our calculation and in MCFM as well.

The total cross sections are comparable in magnitude, though they differ considerably: 0.406 nb in $k_\perp$-factorization and 0.748 nb in collinear factorization.

The transverse momentum distribution of the vector boson are shown in Fig. 9. The comparison of the $k_\perp$-factorization approach to the collinear shows that they agree in transversal momentum distributions of Z at high values of this quantity. This is no surprise, since at high $p_{Z\perp}$ the contribution from initial state gluon transverse momenta is expected to become small.

In the distribution of the azimuthal angular distance of Z and $\max(p_{b,\perp}, p_{\bar{b},\perp})$ (Fig. 10) we observe that the region from 0 to $\pi/2$ is forbidden within the collinear calculation due to momentum conservation, which is not the case for $k_\perp$-factorization. This is caused by the contribution from initial state gluon transversal momentum which allows the transversal momenta of Z, b and $\bar{b}$ to be unbalanced. A larger spread of possible configurations causes that the distribution in the $k_\perp$-factorization calculation flattens.

3 NLO inclusive jet production in $k_\perp$-factorization

Author: Jochen Bartels, Agustin Sabio-Vera, Florian Schwennsen

At different high energy colliders the inclusive jet production is one of the basic measurements. Besides the very successful approach of collinear factorization, also within $k_\perp$-factorization jet production at HERA has been described [60]. There, the jet vertex has been constructed from the central hard matrix element of quark-antiquark production – connected to the unintegrated gluon and the photon being emmitted from the electron. The LO calculation of the corresponding $\gamma^* g \to q\bar{q}$ matrix element is straightforward and contains just two diagrams – one sample is shown in Fig. 11a. As it was shown in Ref. [61], $k_\perp$-factorization in the small x regime can be formulated at NLO accuracy. However, the jet production at HERA has not been calculated at NLO accuracy so far, but the building blocks are contained in the calculation of the NLO photon impact factor [62–66] including virtual corrections (like in Fig. 11b) and
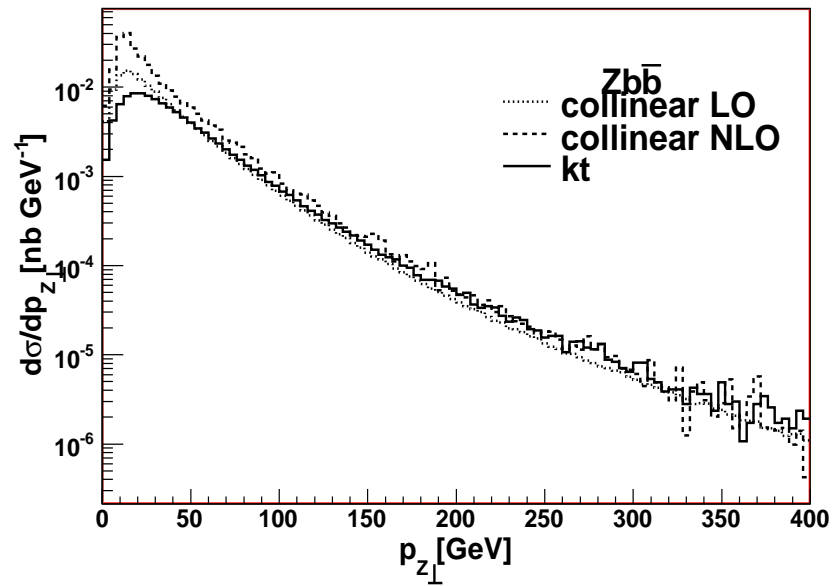
Fig. 9: Comparison of cross sections differential in transverse momentum of the produced Z gauge boson. Calculation with massless b-quarks.
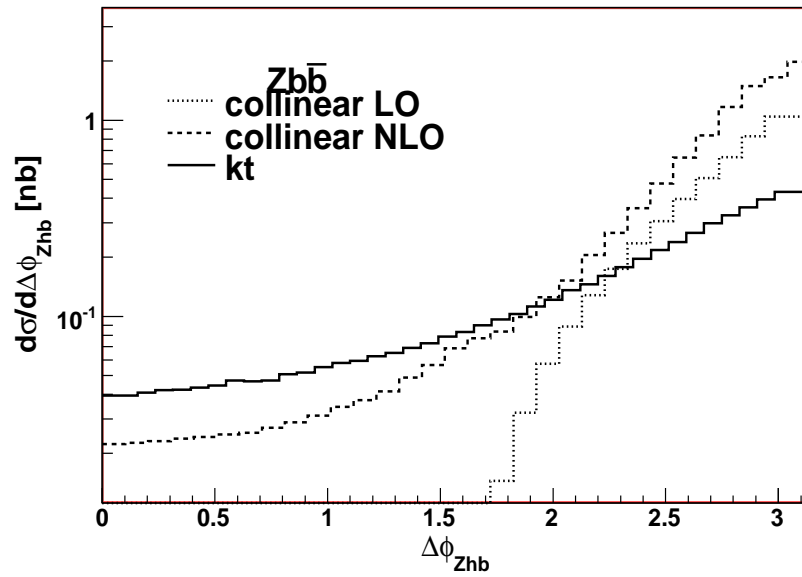

Fig. 10: Comparison of cross sections differential in distance in azimuthal angle of Z and higher $p_\perp$ $b/\bar{b}$. Calculation with massless b-quarks.
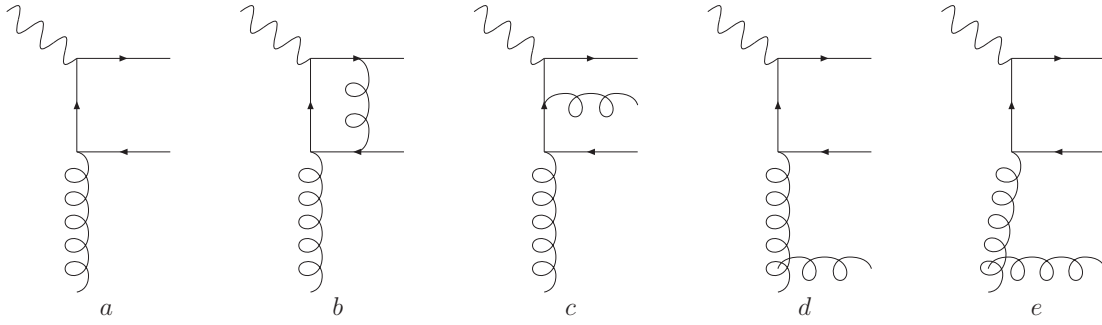
Fig. 11: sample diagrams for the dijet vertex in DIS.

corrections due to the emission of an additional gluon. For such a gluon one has to separate the case where the gluon is 'close' to the vertex, giving a standard real correction to the process (like in Fig. 11c), or where the gluon is 'well separated' from the vertex (like indicated in Fig. 11d). Another contribution (symbolically indicated in Fig. 11e) would come from the different energy scales at the jet and the proton vertices. The nature of these latter corrections will become more clear when we discuss in the following the jet vertex for hadron-hadron scattering.

In $k_\perp$-factorization of hadron-hadron collisions, the jet emission vertex can be identified with the Reggeon-Reggeon-gluon vertex (indicated in Fig. 12a). Its square is nothing else but the LO BFKL-kernel. Since the BFKL equation – from which $k_\perp$-factorization can be derived – has been formulated at NLO [67, 68] as well, it is also possible to calculate the jet emission vertex at this order [61] taking into account that at NLO also the Reggeon-Reggeon-gluon-gluon and Reggeon-Reggeon-quark-antiquark vertices enter the game. It is not sufficient to simply start from the fully integrated emission vertex as used in the NLO BFKL kernel [67, 68]. Rather, one has to carefully separate all the different contributions in their unintegrated form before one can combine them. Moreover, special care has to be taken on the correct treatment of the energy scales involved.

Instead of deriving in detail all the formulas, let us focus on the nature of the different contributions to the NLO jet vertex. In Fig. 12 we represent the different types of contributions by a symbolic diagram. At NLO virtual corrections to the vertex enter the game as shown in Fig. 12b. Since off-shell amplitudes per se are not gauge invariant, the calculation has to be performed as an embedded process. One can *e.g.* consider the process $q+q \to q+g+q$ in multi-Regge-kinematics and extract the off-shell Reggeon-Reggeon-gluon vertex. Virtual corrections to this process then also include diagrams (like box diagrams) which do not factorize individually but only in the sum. Therefore, Fig. 12b can only be regarded as one specific example of a virtual correction.

The real corrections to the one jet production consist of two gluon and quark-antiquark production. For the quark-antiquark production one just has to distinguish two cases: either both
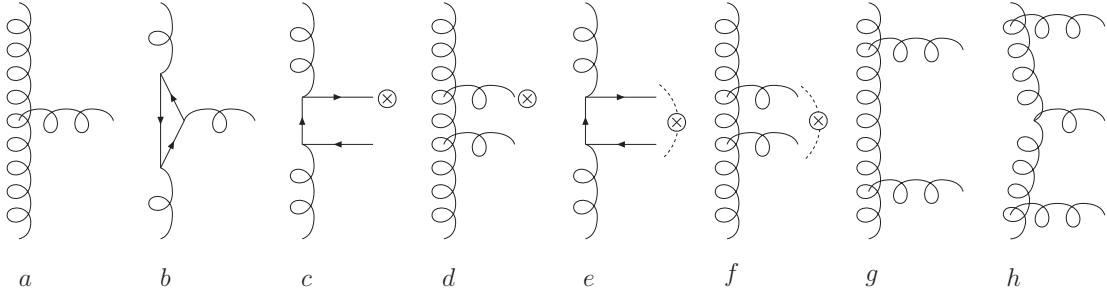
Fig. 12: sample diagrams for the jet vertex in pp.

particles are 'well separated' and only one forms the jet while the other contributes to the inclusive part (Fig. 12c), or they are 'close to each other' and form one jet (Fig. 12e). The question, whether they are 'well separated' or 'close to each other', has to be answered by a specific jet definition. The same distinction has to be made for the two gluon production (Fig. 12d and Fig. 12f).

However, the two-gluon production involves some subtleties. Even if the two gluons cannot be combined in one jet, there still remains the question whether the gluon belongs to the same emission vertex or to different ones. A more detailed study of the arrangement of diagrams in the complete framework of NLO BFKL [61, 69] reveals that a contribution from the two neighbored rungs (Fig. 12g) has to be reorganized into the NLO vertex at hand. The contributions in Fig. 12d and Fig 12g both depend on the scale s_Λ which separates the multi-Regge-kinematics from the quasi-multi-Regge-kinematics. The inclusion of the contribution in Fig. 12g makes the NLO jet vertex (and the NLO BFKL kernel) – to next-to-leading accuracy – independent of s_Λ.

The original formulation of the BFKL approach relies on the scattering of two objects providing an intrinsic and similar hard scale. Instead, in our setting we have to deal with the evolution between the proton – at a soft scale – and the jet – at a hard scale. This imbalance 'tilts' the whole evolution such that in fact the BFKL evolution kernel gets a correction introducing some additional collinear evolution. In the language of BFKL this can be understood as the change from a symmetric energy scale s_0 – like $s_0 = \sqrt{Q_1 Q_2}$ for two colliding objects with scales Q_1 and Q_2 respectively – to an asymmetric one $s_0 = k_{\perp,\mathrm{Jet}}^2$. In the end, the result does not depend on this artificial energy scale s_0, which is ensured by compensating corrections to the impact factors. With respect to the gluon ladder, our jet vertex acts as a kind of impact factor and hence receives from above and below two corrections due to this energy scale change. These complex dependencies involve a large number of concrete diagrams – we only symbolically mark by Fig. 12h that the tilted gluon evolution leads to a correction of the jet emission vertex.

The virtual corrections (Fig. 12b) themselves are infrared divergent. These divergences are canceled by the real corrections (Fig. 12c-f) after they are integrated over. To obtain a jet vertex which is explicitly free of divergences, additional effort has to be made. After identification of those terms in the real corrections which will lead to divergences, one can compensate them by an unintegrated subtraction term, while the integrated subtraction term (which in fact is added such that effectively the result is not changed) cancels the explicit divergences of the virtual

corrections. The exact form of this subtraction term as well as all other formulas which are needed can be found in Ref. [61].

4 Multijet production in the multi-Regge limit: Mueller–Navelet and forward jets

Authors: Agustín Sabio Vera, Florian Schwennsen

In this section we briefly describe the calculations performed in [70–73] to obtain the azimuthal angle correlations in Mueller–Navelet jets [74] and forward jets at HERA using the Balitsky–Fadin–Kuraev–Lipatov (BFKL) equation in the next–to–leading (NLO) approximation [67,68] (see also [75–78]). We first comment on the normalized differential cross section for Mueller–Navelet jets. As it is quite insensitive to the parton distribution functions we can simply operate with partonic cross sections, *i.e.*

$$\frac{d\hat{\sigma}}{d^2\vec{q}_1 d^2\vec{q}_2} = \frac{\pi^2\bar{\alpha}_s^2}{2}\frac{1}{q_1^2 q_2^2}\int\frac{d\omega}{2\pi i}e^{\omega Y}f_\omega\left(\vec{q}_1,\vec{q}_2\right), \tag{12}$$

where $\bar{\alpha}_s = \alpha_s N_c/\pi$, $\vec{q}_{1,2}$ are the transverse momenta of the tagged jets, and Y their relative rapidity. The Green's function carries the bulk of the Y dependence and is the solution to the NLO BFKL equation,

$$\left(\omega - \bar{\alpha}_s\hat{K}_0 - \bar{\alpha}_s^2\hat{K}_1\right)\hat{f}_\omega = \hat{1}, \tag{13}$$

which acts on the basis including the azimuthal angle, *i.e.*,

$$\langle\vec{q}|\,\nu,n\rangle = \frac{1}{\pi\sqrt{2}}\left(q^2\right)^{i\nu-\frac{1}{2}}e^{i n\theta}. \tag{14}$$

As Y increases the azimuthal angle dependence is controlled by the kernel and it is then reasonable to use LO jet vertices which are much simpler than the NLO ones [79, 80]. The differential cross section in the azimuthal angle $\phi = \theta_1 - \theta_2 - \pi$, with θ_i being the angles of the two tagged jets, reads

$$\frac{d\hat{\sigma}\left(\alpha_s, Y, p_{1,2}^2\right)}{d\phi} = \frac{\pi^2\bar{\alpha}_s^2}{4\sqrt{p_1^2 p_2^2}}\sum_{n=-\infty}^{\infty}e^{i n\phi}\mathcal{C}_n\left(Y\right), \tag{15}$$

where p_1 and p_2 are the cuts on transverse momenta and

$$\mathcal{C}_n\left(Y\right) = \frac{1}{2\pi}\int_{-\infty}^{\infty}\frac{d\nu}{\left(\frac{1}{4}+\nu^2\right)}\left(\frac{p_1^2}{p_2^2}\right)^{i\nu}e^{\chi\left(|n|,\frac{1}{2}+i\nu,\bar{\alpha}_s(p_1 p_2)\right)Y}, \tag{16}$$

and the NLO kernel can be written as

$$\chi\left(n,\gamma,\bar{\alpha}_s\right) = \bar{\alpha}_s\chi_0\left(n,\gamma\right) + \bar{\alpha}_s^2\left(\chi_1\left(n,\gamma\right) - \frac{\beta_0}{8N_c}\frac{\chi_0\left(n,\gamma\right)}{\gamma\left(1-\gamma\right)}\right). \tag{17}$$

The eigenvalue of the LO kernel is $\chi_0\left(n,\gamma\right) = 2\psi\left(1\right) - \psi\left(\gamma + \frac{n}{2}\right) - \psi\left(1 - \gamma + \frac{n}{2}\right)$, with ψ the logarithmic derivative of the Euler function. The action of $\hat{K}_1$, in $\overline{\text{MS}}$ scheme, can be found in [81]. The full cross section only depends on the $n = 0$ component,

$$\hat{\sigma} = \frac{\pi^3\bar{\alpha}_s^2}{2\sqrt{p_1^2 p_2^2}}\mathcal{C}_0\left(Y\right). \tag{18}$$

The average of the cosine of the azimuthal angle times an integer projects out the contribution from each of these angular components:

$$\frac{\langle \cos(m\phi) \rangle}{\langle \cos(n\phi) \rangle} = \frac{\mathcal{C}_m(Y)}{\mathcal{C}_n(Y)}. \tag{19}$$

The normalized differential cross section is

$$\frac{1}{\hat{\sigma}} \frac{d\hat{\sigma}}{d\phi} = \frac{1}{2\pi} \sum_{n=-\infty}^{\infty} e^{in\phi} \frac{\mathcal{C}_n(Y)}{\mathcal{C}_0(Y)} = \frac{1}{2\pi} \left\{ 1 + 2 \sum_{n=1}^{\infty} \cos(n\phi) \langle \cos(n\phi) \rangle \right\}. \tag{20}$$

The BFKL resummation is not stable at NLO for zero conformal spin. A manifestation of this lack of convergence is what we found in the gluon–bremsstrahlung scheme where our NLO distributions have an unphysical behavior whenever the $n = 0$ conformal spin appears in the calculation. To solve this problem we imposed compatibility with renormalization group evolution in the DIS limit following [82–84] for all conformal spins. The new kernel with collinear improvements to all orders in the coupling reads [70–73]

$$\begin{aligned}
\omega = {} & \bar{\alpha}_s \left(1 + \mathcal{A}_n \bar{\alpha}_s\right) \left\{ 2\psi(1) - \psi\left(\gamma + \frac{|n|}{2} + \frac{\omega}{2} + \mathcal{B}_n \bar{\alpha}_s\right) \right. \\
& \left. - \psi\left(1 - \gamma + \frac{|n|}{2} + \frac{\omega}{2} + \mathcal{B}_n \bar{\alpha}_s\right) \right\} + \bar{\alpha}_s^2 \left\{ \chi_1(|n|, \gamma) - \frac{\beta_0}{8N_c} \frac{\chi_0(n, \gamma)}{\gamma(1-\gamma)} \right. \\
& \left. - \mathcal{A}_n \chi_0(|n|, \gamma) + \left(\psi'\left(\gamma + \frac{|n|}{2}\right) + \psi'\left(1 - \gamma + \frac{|n|}{2}\right)\right) \left(\frac{\chi_0(|n|, \gamma)}{2} + \mathcal{B}_n\right) \right\}, \tag{21}
\end{aligned}$$

where $\mathcal{A}_n$ and $\mathcal{B}_n$ are collinear coefficients [70–73]. After this extra resummation our observables have a good physical behavior and are independent of the renormalization scheme. However, it is very important to stress that the asymptotic behavior of the BFKL resummation is convergent for non zero conformal spins. This is why we propose that the ideal distributions to investigate BFKL effects experimentally are those of the form $\langle \cos(m\phi) \rangle / \langle \cos(n\phi) \rangle$ with $m, n \neq 0$, we will see below that in this case the difference between the predictions at LO and at higher orders results is very small.

4.1 Mueller–Navelet jets at the LHC

Long ago, the DØ [85] collaboration analyzed data for Mueller–Navelet jets at $\sqrt{s} = 630$ and 1800 GeV. For the angular correlation, LO BFKL predictions were first obtained in [86, 87] and failed to describe the data since the LO results were far too decorrelated. On the other hand, a more conventional fixed order NLO analysis using JETRAD underestimated the decorrelation, while HERWIG was in agreement with the data.

In Fig. 13 we compare the Tevatron data for $\langle \cos\phi \rangle = \mathcal{C}_1/\mathcal{C}_0$ with our LO, NLO and collinearly resummed predictions. For Tevatron's cuts, where the lower cut off in transverse momentum for one jet is 20 GeV and for the other 50 GeV, the NLO calculation is instable under renormalization scheme changes. The convergence of our observables is poor whenever the coefficient associated to zero conformal spin, $\mathcal{C}_0$, is used in the calculation. If we eliminate
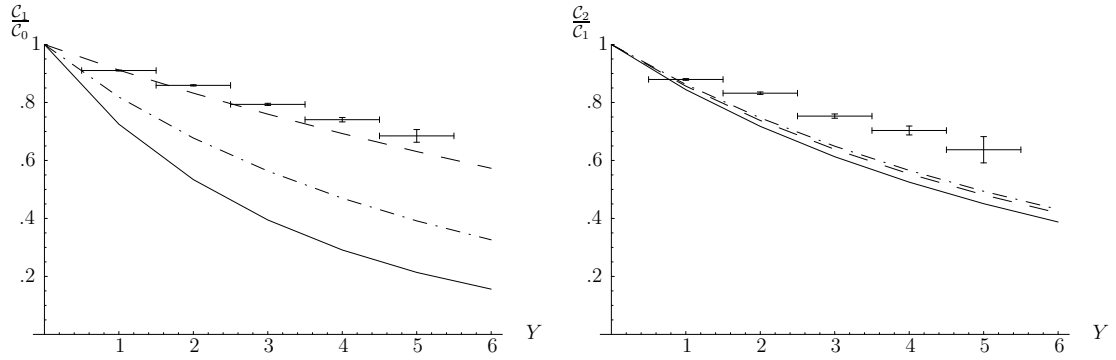
Fig. 13: Left: $\langle \cos \phi \rangle = \mathcal{C}_1/\mathcal{C}_0$ and Right: $\frac{\langle \cos 2\phi \rangle}{\langle \cos \phi \rangle} = \frac{\mathcal{C}_2}{\mathcal{C}_1}$, at a $p\bar{p}$ collider with $\sqrt{s} = 1.8$ TeV for BFKL at LO (solid) and NLO (dashed). The results from the resummation presented in the text are shown as well (dash–dotted).

this coefficient by calculating the ratios defined in Eq. (19) then the predictions are very stable, see Fig. 13.

The full angular dependence studied at the Tevatron by the D∅ collaboration was published in [85]. In Fig. 14 we compare this measurement with the predictions obtained in our approach. For the differential cross section we also make predictions for the LHC at larger Y in Fig. 15. We estimated several uncertainties in our approach which are represented by gray bands.
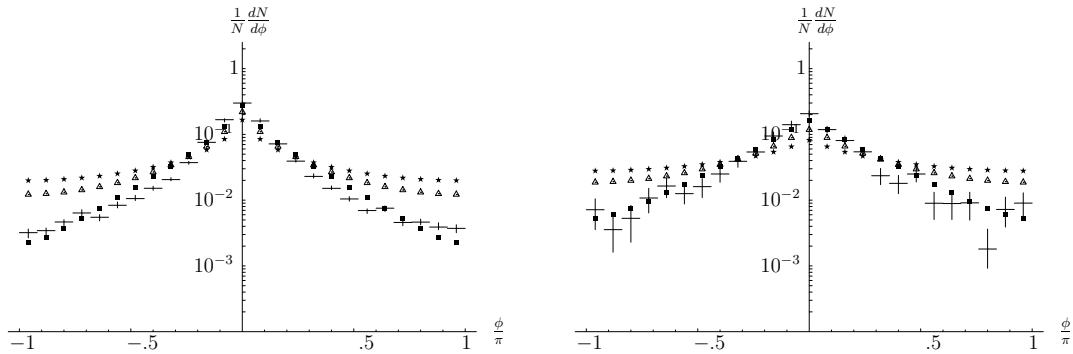

Fig. 14: $\frac{1}{N}\frac{dN}{d\phi}$ in a $p\bar{p}$ collider at $\sqrt{s}$=1.8 TeV using a LO (stars), NLO (squares) and resummed (triangles) BFKL kernel. Plots are shown for Y = 3 (left) and Y = 5 (right).

4.2 Forward jets at HERA

In this section we apply the BFKL formalism to predict the decorrelation in azimuthal angle between the electron and a forward jet associated to the proton in Deep Inelastic Scattering (DIS). When the separation in rapidity space between the scattered electron and the forward jet is large and the transverse momentum of the jet is similar to the virtuality of the photon resolving the hadron, then the dominant terms are of BFKL type. This process is similar to that of Mueller–Navelet jets, the only difference being the substitution of one jet vertex by the vertex describing
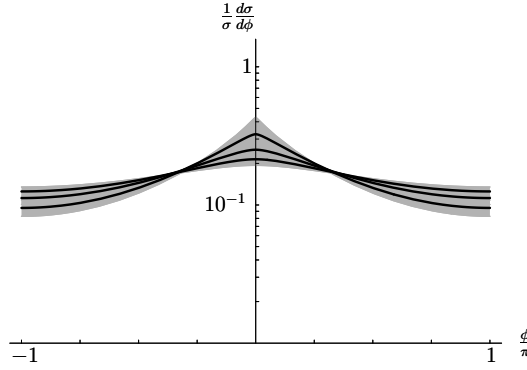
Fig. 15: $\frac{1}{\sigma}\frac{d\sigma}{d\phi}$ in our resummation scheme for rapidities Y = 7, 9, 11 from top to bottom. The gray band reflects the uncertainty in s_0 and in the renormalization scale μ.

the coupling of the electron to the BFKL gluon Green's function via a quark–antiquark pair. Azimuthal angles in forward jets were studied at LO in [88]. We improved their calculation by considering the NLO BFKL kernel and collinear improved versions of it. Fixed order calculations can be found in [89].

In the production of a forward jet in DIS it is necessary to extract a jet with a large longitudinal momentum fraction x_{FJ} from the proton. When this jet is characterized by a hard scale in the form of a large p_t it is possible to use conventional collinear factorization to describe the process and the production rate may be written as

$$\sigma(s) \;=\; \int dx_{\text{FJ}}\; f_{\text{eff}}(x_{\text{FJ}}, \mu_F^2)\hat{\sigma}(\hat{s}), \tag{22}$$

with $\hat{\sigma}(\hat{s})$ denoting the partonic cross section, and the effective parton density [90] being

$$f_{\text{eff}}(x, \mu_F^2) \;=\; G(x, \mu_F^2) + \frac{4}{9}\sum_f \left[Q_f(x, \mu_F^2) + \bar{Q}_f(x, \mu_F^2) \right], \tag{23}$$

where the sum runs over all quark flavors, and μ_F stands for the factorization scale.

The final expression for the cross section at hadronic level is of the form

$$\frac{d\sigma}{d\text{Y}\, d\phi} \;=\; C_0(\text{Y}) + C_2(\text{Y})\cos 2\phi, \tag{24}$$

with

$$C_n(\text{Y}) \;=\; \frac{\pi^2\bar{\alpha}_s^2}{2}\int_{\text{cuts}} dx_{\text{FJ}}\, dQ^2\, dy\, f_{\text{eff}}(x_{\text{FJ}}, Q^2) B^{(n)}(y, Q^2, \text{Y})\delta\left(x_{\text{FJ}} - \frac{Q^2 e^{\text{Y}}}{ys} \right), \tag{25}$$

where the index in the integral sign refers to the cuts

$$20\ \text{GeV}^2 < Q^2 < 100\ \text{GeV}^2,\quad 0.05 < y < 0.7,\quad 5\cdot 10^{-3} > x_{\text{Bj}} > 4\cdot 10^{-4}. \tag{26}$$

The integration over the longitudinal momentum fraction x_{FJ} of the forward jet involves a delta function fixing the rapidity $Y = \ln x_{\mathrm{FJ}}/x_{\mathrm{Bj}}$ and $B^{(n)}$ is a complicated function which can be found in [70–73].

Since the structure of the electron vertex singles out the components with conformal spin 0 and 2, the number of observables related to the azimuthal angle dependence is limited when compared to the Mueller–Navelet case. The most relevant observable is the dependence of the average $< \cos 2\phi > = C_2/C_0$ with the rapidity difference between the forward jet and outgoing lepton. It is natural to expect that the forward jet will be more decorrelated from the leptonic system as the rapidity difference is larger since the phase space for further gluon emission opens up. This is indeed what we observe in our numerical results shown in Fig. 16. We find similar results to the Mueller–Navelet jets case where the most reliable calculation is that with a collinearly–improved kernel. The main effect of the higher order corrections is to increase the azimuthal angle correlation for a given rapidity difference, while keeping the decrease of the correlation as Y grows.
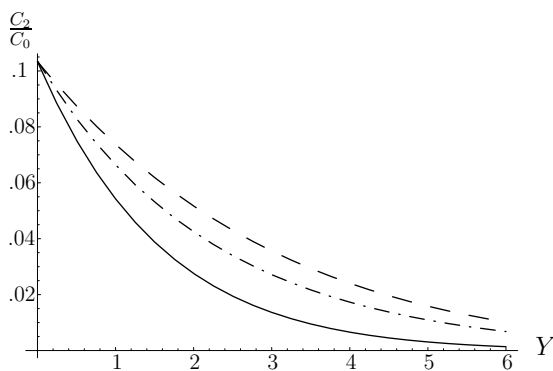

Fig. 16: $< \cos 2\phi >$ at the ep collider HERA at leading (solid), next to leading order (dashed), and for resummed kernel (dash-dotted).

5 NLL BFKL effects: Mueller-Navelet and forward jets

Author: Christophe Royon

5.1 Forward jets at HERA

Following the successful BFKL [91–93] parametrisation of the forward-jet cross-section $d\sigma/dx$ at Leading Order (LO) at HERA [75, 94, 95], it is possible to perform a similar study using Next-to-leading (NLL) resummed BFKL kernels. This method can be used for forward jet production at HERA in particular, provided one takes into account the right two scales of the forward-jet problem, namely Q^2 for the lepton and k_T^2 for the jet vertex respectively. In this short report, we will only discuss the phenomelogical aspects and all detailed calculations can be found in Ref. [71, 73, 76, 77] for forward jets at HERA and in Ref. [78] for Mueller-Navelet jets at the Tevatron and the LHC.
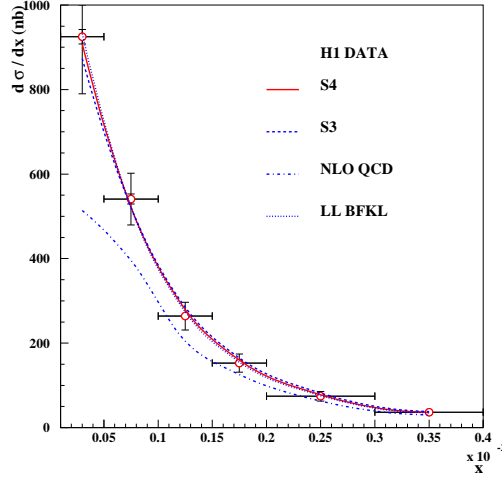
Fig. 17: Comparison between the H1 $d\sigma/dx$ measurement with predictions for BFKL-LL, BFKL-NLL (S3 and S4 schemes) and DGLAP NLO calculations (see text). S4, S3 and LL BFKL cannot be distinguished on that figure.

The BFKL NLL [67, 68, 96] longitudinal transverse cross section reads:

$$\frac{d\sigma_{T,L}^{\gamma*p\to JX}}{dx_J dk_T^2} = \frac{\alpha_s(k_T^2)\alpha_s(Q^2)}{k_T^2 Q^2} f_{eff}(x_J, k_T^2) \int d\gamma \left(\frac{Q^2}{k_T^2}\right)^\gamma \phi_{T,L}^\gamma(\gamma) \, e^{\bar{\alpha}(k_T Q)\chi_{eff}[\gamma,\bar{\alpha}(k_T Q)]Y} \quad (27)$$

where the χ_{eff} is the effective BFKL NLL kernel and the ϕ are the transverse and longitudinal impact factors taken at LL. The effective kernel $\chi_{eff}(\gamma, \bar{\alpha})$ is defined from the NLL kernel $\chi_{NLL}(\gamma, \omega)$ by solving the implicit equation numerically

$$\chi_{eff}(\gamma, \bar{\alpha}) = \chi_{NLL}\left[\gamma, \bar{\alpha}\,\chi_{eff}(\gamma, \bar{\alpha})\right] \ . \quad (28)$$

The integration over γ in Eq. 27 is performed numerically. It is possible to fit directly $d\sigma/dx$ measured [97] by the H1 collaboration using this formalism with one single parameter, the normalisation. The values of χ_{NLL} are taken at NLL [67,68,96] using different resummation schemes to remove spurious singularities defined as S3 and S4 [82]. Contrary to LL BFKL, it is worth noticing that the coupling constant α_S is taken using the renormalisation group equations, the only free parameter in the fit being the normalisation.

To compute $d\sigma/dx$ in the experimental bins, we need to integrate the differential cross section on the bin size in Q^2, x_J (the momentum fraction of the proton carried by the forward jet), k_T (the jet transverse momentum), while taking into account the experimental cuts. To simplify the numerical calculation, we perform the integration on the bin using the variables where the cross section does not change rapidly, namely k_T^2/Q^2, $\log 1/x_J$, and $1/Q^2$. Experimental cuts are treated directly at the integral level (the cut on $0.5 < k_T^2/Q^2 < 5$ for instance) or using a toy Monte Carlo. More detail can be found about the fitting procedure in Appendix A of Ref. [75].

The NLL fits [71, 73, 76, 77] can nicely describe the H1 data [97] for the S4 and S3 schemes [71, 73, 75–77, 94, 95] ($\chi^2 = 0.48/5$ and $\chi^2 = 1.15/5$ respectively per degree of

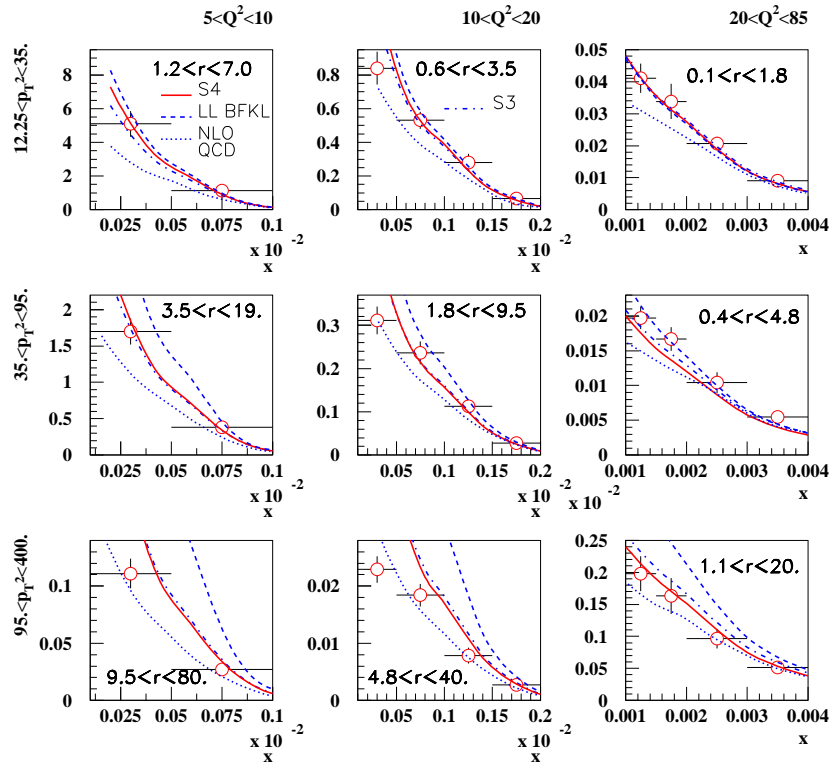**d σ/dx dp$_T^2$ d Q^2 - H1 DATA**

Fig. 18: Comparison between the H1 measurement of the triple differential cross section with predictions for BFKL-LL, BFKL-NLL and DGLAP NLO calculations (see text).

freedom with statistical and systematic errors added in quadrature). The curve using a LL fit is indistinguishable in Fig. 17 from the result of the BFKL-NLL fit. The DGLAP NLO calculation fails to describe the H1 data at lowest x (see Fig. 17). We also checked the effect of changing the scale in the exponential of Eq. 27 from $k_T Q$ to $2k_T Q$ or $k_T Q/2$ which leads to a difference of 20% on the cross section while changing the scale to k_T^2 or Q^2 modifies the result by less than 5% which is due to the cut on $0.5 < k_T^2/Q^2 < 5$. Implementing the higher-order corrections in the impact factor due to exact gluon dynamics in the $\gamma^* \to q\bar{q}$ transition [98] changes the result by less than 3%.

The H1 collaboration also measured the forward jet triple differential cross section [97] and the results are given in Fig. 18. We keep the same normalisation coming from the fit to $d\sigma/dx$ to predict the triple differential cross section. The BFKL LL formalism leads to a good description of the data when $r = k_T^2/Q^2$ is close to 1 and deviates from the data when r is further away from 1. This effect is expected since DGLAP radiation effects are supposed to occur when the ratio between the jet k_T and the virtual photon Q^2 are further away from 1. The BFKL NLL calculation including the Q^2 evolution via the renormalisation group equation leads to a good description of the H1 data on the full range. We note that the higher order corrections are small when $r \sim 1$, when the BFKL effects are supposed to dominate. By contrast, they are significant as expected when r is different from one, i.e. when DGLAP evolution becomes relevant. We notice that the DGLAP NLO calculation fails to describe the data when $r \sim 1$, or in the region where BFKL resummation effects are expected to appear.

In addition, we checked the dependence of our results on the scale taken in the exponential of Eq. 27. The effect is a change of the cross section of about 20% at low p_T increasing to 70% at highest p_T. Taking the correct gluon kinematics in the impact factor lead as expected to a better description of the data at high p_T [71, 73, 76, 77].

5.2 Mueller-Navelet jets at the Tevatron and the LHC

Mueller-Navelet jets are ideal processes to study BFKL resummation effects [74]. Two jets with a large interval in rapidity and with similar tranverse momenta are considered. A typical observable to look for BFKL effects is the measurement of the azimuthal correlations between both jets. The DGLAP prediction is that this distribution should peak towards π - i.e. jets are back-to-back- whereas multi-gluon emission via the BFKL mechanism leads to a smoother distribution. The relevant variables to look for azimuthal correlations are the following:

$$
\begin{aligned}
\Delta\eta &= y_1 - y_2 \\
y &= (y_1 + y_2)/2 \\
Q &= \sqrt{k_1 k_2} \\
R &= k_2/k_1
\end{aligned}
$$

The azimuthal correlation for BFKL reads:

$$
2\pi \, \frac{d\sigma}{d\Delta\eta dR d\Delta\Phi} \bigg/ \frac{d\sigma}{d\Delta\eta dR} = 1 + \frac{2}{\sigma_0(\Delta\eta, R)} \sum_{p=1}^{\infty} \sigma_p(\Delta\eta, R) \cos(p\Delta\Phi)
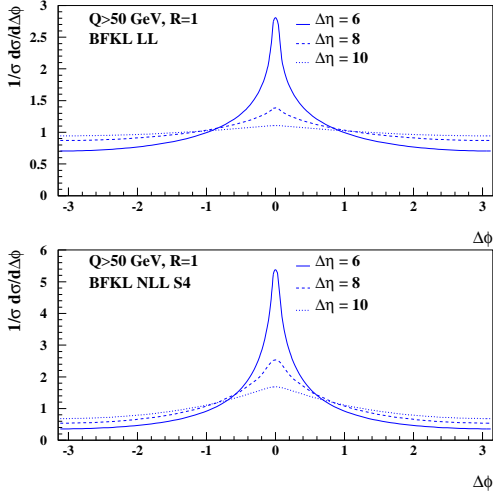$$

Fig. 19: The Mueller-Navelet jet $\Delta\Phi$ distribution for LHC kinematics in the BFKL framework at LL (upper plots) and NLL-S4 (lower plots) accuracy for $\Delta\eta = 6, 8, 10$.
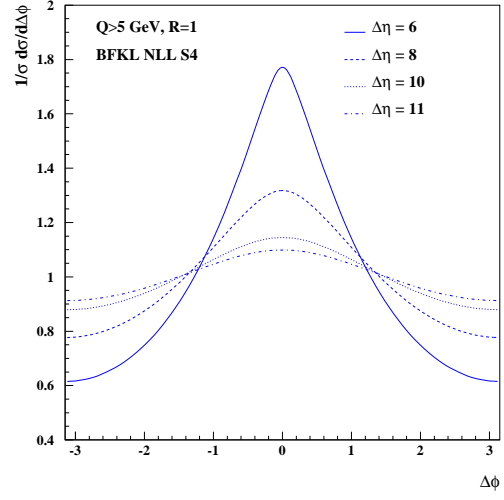
Fig. 20: Azimuthal correlations between jets with $\Delta\eta = 6, 8, 10$ and 11 and $p_T > 5$ GeV in the CDF acceptance. This measurement will represent a clear test of the BFKL regime.

where in the NLL BFKL framework,

$$
\sigma_p = \int_{E_T}^{\infty} \frac{dQ}{Q^3} \alpha_s(Q^2/R)\alpha_s(Q^2 R) \left(\int_{y_<}^{y_>} dy x_1 f_{eff}(x_1, Q^2/R) x_2 f_{eff}(x_2, Q^2 R) \right)
$$
$$
\int_{1/2-\infty}^{1/2+\infty} \frac{d\gamma}{2i\pi} R^{-2\gamma} e^{\bar{\alpha}(Q^2)\chi_{eff}(p,\gamma,\bar{\alpha})\Delta\eta}
$$

and χ_{eff} is the effective resummed kernel. Computing the different σ_p at NLL for the resummation schemes S3 and S4 allowed us to compute the azimuthal correlations at NLL. As expected, the $\Delta\Phi$ dependence is less flat than for BFKL LL and is closer to the DGLAP behaviour [78]. In Fig. 19, we display the observable $1/\sigma d\sigma/d\Delta\Phi$ as a function of $\Delta\Phi$, for LHC kinematics. The results are displayed for different values of $\Delta\eta$ and at both LL and NLL accuracy using the S4 resummation scheme. In general, the $\Delta\Phi$ spectra are peaked around $\Delta\Phi = 0$, which is indicative of jet emissions occuring back-to-back. In addition the $\Delta\Phi$ distribution flattens with increasing $\Delta\eta = y_1 - y_2$. Note the change of scale on the vertical axis which indicates the magnitude of the NLL corrections with respect to the LL-BFKL results. The NLL corrections slow down the azimuthal angle decorrelations for both increasing $\Delta\eta$ and R deviating from 1. We also studied the R dependence of our prediction which is quite weak [78]. We also studied the scale dependence of our results by modifying the scale Q^2 to either $Q^2/2$ or $2Q^2$ and the effect on the azimuthal distribution is of the order of 20%. The effect of the energy conservation in the BFKL equation [78] is large when R goes away from 1. The effect is to reduce the effective value of $\Delta\eta$ between the jets and thus the decorrelation effect. However, it is worth noticing that this effect is negligible when R is close to 1 where this measurement will be performed.

A measurement of the cross-section $d\sigma^{hh\to JXJ}/d\Delta\eta dR d\Delta\Phi$ at the Tevatron (Run 2) or

the LHC will allow for a detailed study of the BFKL QCD dynamics since the DGLAP evolution leads to much less jet angular decorrelation (jets are back-to-back when R is close to 1). In particular, measurements with values of $\Delta\eta$ reaching 8 or 10 will be of great interest, as these could allow to distinguish between BFKL and DGLAP resummation effects and would provide important tests for the relevance of the BFKL formalism.

To illustrate this result, we give in Fig. 20 the azimuthal correlation in the CDF acceptance. The CDF collaboration installed the mini-Plugs calorimeters aiming for rapidity gap selections in the very forward regions and these detectors can be used to tag very forward jets. A measurement of jet p_T with these detectors would not be possible but their azimuthal segmentation allows a ϕ measurement. In Fig. 20, we display the jet azimuthal correlations for jets with a $p_T > 5$ GeV and $\Delta\eta =$6, 8, 10 and 11. For $\Delta\eta =$11, we notice that the distribution is quite flat, which would be a clear test of the BFKL prediction.

6 Forward Jets in the CASTOR calorimeter in the CMS experiment

Author: Albert Knutsson

The CASTOR (Centauro and STrange Object Research) detector [99] is a Cherenkov radiation calorimeter consisting of tungsten absorber plates sandwitched with plates of quartz, used as the active material in the detector. The construction is repeated in octants in azimuthal angle, giving a full 360° coverage. For each ocant lightguides and photomultipliers are situated on top of the plates in two coloumns, 14 channels deep along the beam direction. 2 of the 14 channels are designed for detection of electromagnetic particles and the rest are hadronic channels. Thus the detector consists of a total number of 16x14 channels. CASTOR is situated 14.4 m from the interaction vertex in the CMS detector at LHC and covers the pseudorapidity range $5.2 < \eta < 6.6$.

Since CASTOR has no segmentation in polar angle it will not be possible to define jets according to conventional jet algorithms which use the energy, polar and azimuthal angle of particles. Here we investigate the possiblity to measure jet events with CASTOR, by using only the azimuthal segmenation and energy deposition. The studies are carried out on Monte Carlo generator level. Events are generated with the ARIADNE event generator [100], with the hadron level jets defined according to the inclusive k_T algorithm. The kinematic region has been divided into 16 slices in phi, for which the energies of all particles are summed. In Fig. 21a-b the correlations between the hadron level jet energy and different energy depositions in the CASTOR region are shown. Clearly the total energy contained in the CASTOR region is too large compared to the energy of the hadron level jet (Fig. 21a), while the energy in the phi segment with highest energy gives a better correlation with the true jet energy (Fig. 21b). The best reconstruction of the jet energy is achieved if the energy in the most active phi segmenet is summed with the two neighbouring cells (Fig. 21c). This is the method we use in the physics studies presented in the next section. In future, one can improve the jet reconstruction with more complex algorithms in order to obtain an even better correlation in jet energy. Finally, in Fig. 22 the azimuthal angle of the jet axis is plotted versus the azimuthal slice with highest energy. A good correlation is seen.

Events in which an energetic jet is produced close to the proton remnant (the forward direction) are sensitive to the higher order reactions due to the long rapidity range available for
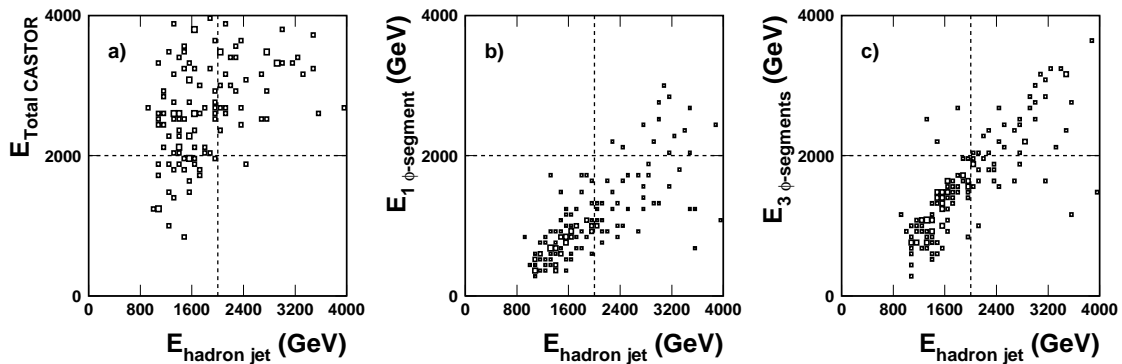
Fig. 21: Monte Carlo predictions on generator level for the hadron level jet energy vs. **a** the energy contained in the full CASTOR region, **b** the energy in the ϕ-segment with the highest energy deposit and **c** the energy in the ϕ-segment with the highest energy deposit summed with the energy in two neighbouring cells.
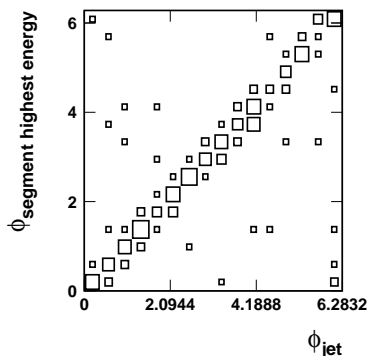

Fig. 22: Azimuthal angle of the highest energy ϕ-segment vs. the azimuthal angle of the jet.

radiation between the jet and the hard scattering vertex. The longitudinal momentum fraction of the proton, x, can be related to the rapidity, y, by approximately $x \sim e^{-y}$, which further suggests that forward physics gives us valuable information about low x parton dynamics.

At HERA, forward jet events have been analysed [97,101] and improved our understanding of QCD. Available fixed order calculations (next-to-leading order $O(\alpha_s^2)$) as well as the higher order reactions approximated by DGLAP parton showers underestimate the HERA data by up to a factor of 2. The data can be described only if the ordering of the transverse momenta of the radiated gluons is broken in the theoretical predictions.

In events where the transverse momentum of the forward jet is close to the scale of the hard reaction the DGLAP like scenario, i.e. events with QCD radiation ordered in transverse momenta, is further supressed. In the HERA analysis this is achieved by requiring that the square of the transverse momentum of the forward jet was in the same order as the virtuality of the exchanged photon. In the analysis presented here we instead require that two additional hard jets are produced in the central region of the detector. For the forward jets in the CASTOR region this gives up to 5 units of pseudorapidity range available for more gluon radiation.

For this study the Monte Carlo events are generated by using the full event generators PYTHIA 6.4.14 [9] and ARIADNE 1.4 [100]. PYTHIA 6.4.14 is based on LO DGLAP parton showers, which gives gluon radiation ordered in transverse momentum with respect to rapidity. In ARIADNE, parton showers are generated by the Color Dipole Model (CDM), resulting in gluon radiation without any ordering in transverse momentum with respect to rapidity. This corresponds to a BFKL like final state. PYTHIA is run with the so called tune A multiple interaction model.

The hadron level jets are defined with the inclusive k_t algorithm. Events are selected which contain a jet with a transverse momentum $E_T > 10$ GeV and a pseudorapidity $5.2 < \eta < 6.6$. To further suppress events with DGLAP like dynamics, two jets with $E_T > 10$ GeV are required in the central region, $|\eta| < 1.5$. The resulting cross-section is shown in Fig. 23 as a function of the forward jet energy. As can be seen, CDM is producing more jets at higher energies, while the events with gluon emissions generated according to DGLAP dynamics have a supressed jet production. At the highest forward jet energies the difference between the models is up to two orders of magnitude.

In the following we replace the hadronic forward jet with the jet reconstruction described in the previous section. In addition we have also smeared the particle energies according to resolutions measured in the CASTOR beam test [102] and applied a noise cut at 1 GeV. Since we can no longer determine the E_T of the reconstructed forward jet, this cut is removed from the forward jet selection, but the measured range in energy is kept. The major consequence is, as expected, an increased number of jets at low energies. The predictions from PYTHIA and CDM shows that the very high sensitivity to the scheme used for the QCD radiation is still preserved (see Fig. 24).

In Fig. 25a and b we investigate the PDF uncertainties for the suggested measurement. As can be seen in Fig. 25a the predicted forward jet cross section does not distinguish between PDFs which has been fitted at leading order with LO α_s, CTEQ6L, or NLO α_s, CTEQ6LL. Using the CTEQ6.5 PDF however gives a lower forward jet cross section, as illustrated in Fig. 25b. Here the PDF uncertainty, based on the 40 error eigensets for CTEQ6.5, are shown for the PYTHIA prediction.

Finally, the response to multiple interactions (MI) is studied in Fig. 26. We see that the impact of MI is expected to be large in general; excluding MI lowers the cross section by roughly an order of magnitude. Except of that, the sensitivity to the different MI tunes and models are fairly small in comparison to the impact of using a CDM.

In summary a method for jet reconstuction in the CASTOR calorimeter has been suggested. We have shown that using the method to measure forward jets in CASTOR in addition to two jets in the central region may give a very large sensitity to the dynamics of the parton shower. This is also true if PDF uncertainties and different MI models are taken into account.

References

[1] NLO Multileg Working Group Collaboration, Z. Bern *et al.* (2008),
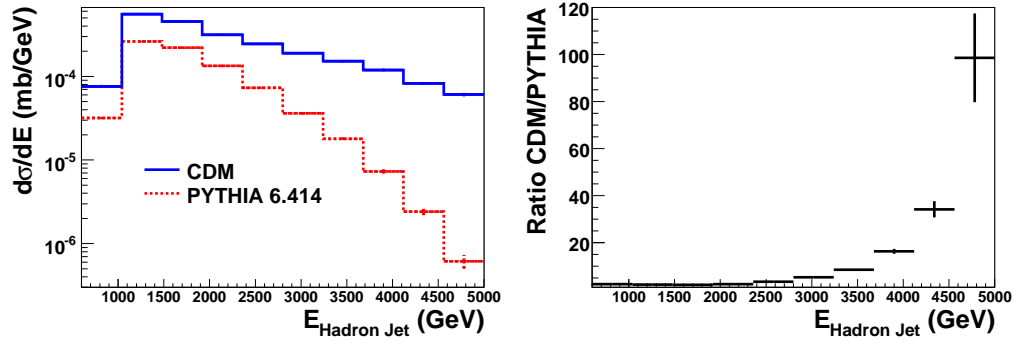   arXiv:0803.0494 [hep-ph].

Fig. 23: Hadron level cross sections for events with two central jets and a forward jet in the pseudorapidity region of the CASTOR calorimeter. The predictions are on generator level wihtout any assumptions about the detector.
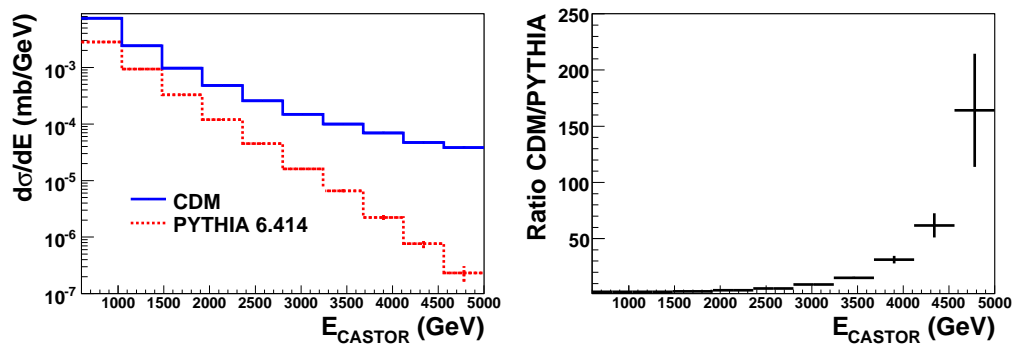

Fig. 24: Cross sections for events with two central jets and a forward jet in the pseudorapidity region of the CASTOR calorimeter. The predictions are on generator level, but here with the forward jet reconstructed as described in the text and forward particle momenta smeared according to CASTOR beam test data.

[2] S. Hoche *et al.* (2006). hep-ph/0602031.

[3] N. Lavesson and L. Lonnblad, JHEP **04**, 085 (2008), `arXiv:0712.2966` `[hep-ph]`.

[4] J. Alwall *et al.*, Eur. Phys. J. **C53**, 473 (2008).

[5] S. Alekhin *et al.* (2005), `arXiv:hep-ph/0601012`.

[6] S. Alekhin *et al.* (2005), `arXiv:hep-ph/0601013`.

[7] G. Corcella *et al.*, JHEP **01**, 010 (2001), `arXiv:hep-ph/0011363`.

[8] G. Corcella *et al.* (2002), `arXiv:hep-ph/0210213`.

[9] T. Sjostrand, S. Mrenna, and P. Skands, JHEP **05**, 026 (2006), `arXiv:hep-ph/0603175`.

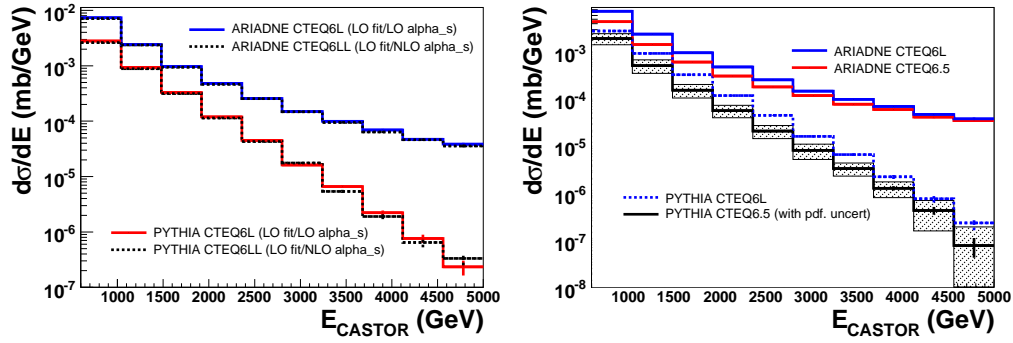[10] G. Marchesini and B. R. Webber, Nucl. Phys. **B386**, 215 (1992).

Fig. 25: The PDF uncertainties for the 2+forward jet cross section. The predictions are on generator level, but with the forward jet reconstructed as described in the text and forward particle momenta smeared according to CASTOR beam test data.
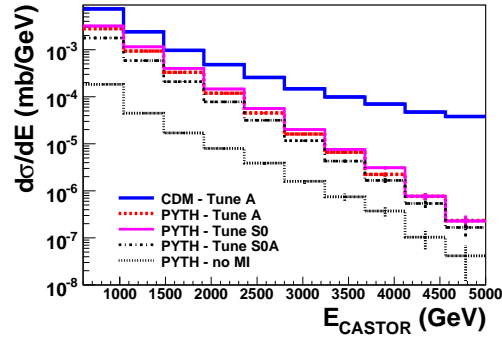

Fig. 26: Monte Carlo prediction for the 2+forward jet cross section using different MI models and tunes. The predictions are on generator level, but with the forward jet reconstructed as described in the text and forward particle momenta smeared according to CASTOR beam test data.

[11] M. Ciafaloni, Nucl. Phys. **B296**, 49 (1988).

[12] S. Catani, M. Ciafaloni, and F. Hautmann, Phys. Lett. **B242**, 97 (1990).

[13] S. Catani, M. Ciafaloni, and F. Hautmann, Nucl. Phys. **B366**, 135 (1991).

[14] S. Catani, M. Ciafaloni, and F. Hautmann, Phys. Lett. **B307**, 147 (1993).

[15] Small x Collaboration, B. Andersson *et al.*, Eur. Phys. J. **C25**, 77 (2002), arXiv:hep-ph/0204115.

[16] H. Jung, Comput. Phys. Commun. **143**, 100 (2002), arXiv:hep-ph/0109102.

[17] H. Jung and G. P. Salam, Eur. Phys. J. **C19**, 351 (2001), arXiv:hep-ph/0012143.

[18] L. Lonnblad and M. Sjodahl, JHEP **05**, 038 (2005), arXiv:hep-ph/0412111.

[19] L. Lonnblad and M. Sjodahl, JHEP **02**, 042 (2004), arXiv:hep-ph/0311252.

[20] G. Gustafson, L. Lonnblad, and G. Miu, JHEP **09**, 005 (2002), arXiv:hep-ph/0206195.

[21] K. J. Golec-Biernat, S. Jadach, W. Placzek, P. Stephens, and M. Skrzypek, Acta Phys. Polon. **B38**, 3149 (2007), arXiv:hep-ph/0703317.

[22] S. Hoche, F. Krauss, and T. Teubner, *Multijet events in the k_T-factorisation scheme*, 2007. arXiv:0705.4577 [hep-ph].

[23] Small x Collaboration, J. R. Andersen *et al.*, Eur. Phys. J. **C35**, 67 (2004), arXiv:hep-ph/0312333.

[24] F. Hautmann and H. Jung (2007), arXiv:0712.0568 [hep-ph].

[25] F. Hautmann and H. Jung, JHEP **10**, 113 (2008), arXiv:0805.1049 [hep-ph].

[26] M. Ciafaloni, PoS **RADCOR2007**, 029 (2007).

[27] G. Altarelli, R. D. Ball, and S. Forte, PoS **RADCOR2007**, 028 (2007), arXiv:0802.0968 [hep-ph].

[28] J. Collins, *Rapidity divergences and valid definitions of parton densities*, 2008. arXiv:0808.2665 [hep-ph].

[29] J. C. Collins (2001), arXiv:hep-ph/0106126.

[30] S. Catani and F. Hautmann, Nucl. Phys. **B427**, 475 (1994), arXiv:hep-ph/9405388.

[31] S. Catani and F. Hautmann, Phys. Lett. **B315**, 157 (1993).

[32] L. N. Lipatov, Phys. Rept. **286**, 131 (1997), arXiv:hep-ph/9610276.

[33] M. Buza, Y. Matiounine, J. Smith, R. Migneron, and W. L. van Neerven, Nucl. Phys. **B472**, 611 (1996), arXiv:hep-ph/9601302.

[34] S. Riemersma, J. Smith, and W. L. van Neerven, Phys. Lett. **B347**, 143 (1995), arXiv:hep-ph/9411431.

[35] E. Laenen, S. Riemersma, J. Smith, and W. L. van Neerven, Nucl. Phys. **B392**, 162 (1993).

[36] S. Moch, J. A. M. Vermaseren, and A. Vogt, Phys. Lett. **B606**, 123 (2005), arXiv:hep-ph/0411112.

[37] A. Vogt, S. Moch, and J. A. M. Vermaseren, Nucl. Phys. **B691**, 129 (2004), arXiv:hep-ph/0404111.

[38] DELPHI Collaboration, P. Abreu *et al.*, Z. Phys. **C73**, 11 (1996).

[39] H1 Collaboration, C. Adloff *et al.*, Eur. Phys. J. **C21**, 33 (2001), hep-ex/0012053.

[40] W. Press *et al*, *Numerical Recipes*. Cambridge University Press, 1992.

[41] F. James and M. Roos, Comput. Phys. Commun. **10**, 343 (1975).

[42] J. C. Collins and R. K. Ellis, Nucl. Phys. **B360**, 3 (1991).

[43] S. Berge, P. M. Nadolsky, F. Olness, and C. P. Yuan, Phys. Rev. **D72**, 033015 (2005), `arXiv:hep-ph/0410375`.

[44] M. Deák and F. Schwennsen, JHEP **09**, 035 (2008), `arXiv:0805.3763 [hep-ph]`.

[45] S. P. Baranov, A. V. Lipatov, and N. P. Zotov, Phys. Rev. **D78**, 014025 (2008), `arXiv:0805.4821 [hep-ph]`.

[46] S. P. Baranov, A. V. Lipatov, and N. P. Zotov, Yad. Fiz. **67**, 856 (2004), `arXiv:hep-ph/0302171`.

[47] A. V. Lipatov and N. P. Zotov, Phys. Rev. **D75**, 014028 (2007), `arXiv:hep-ph/0611302`.

[48] F. Hautmann, Phys. Lett. **B535**, 159 (2002), `arXiv:hep-ph/0203140`.

[49] A. V. Lipatov and N. P. Zotov, Eur. Phys. J. **C44**, 559 (2005), `arXiv:hep-ph/0501172`.

[50] M. A. Kimber, A. D. Martin, and M. G. Ryskin, Phys. Rev. **D63**, 114027 (2001), `hep-ph/0101348`.

[51] G. Watt, A. D. Martin, and M. G. Ryskin, Eur. Phys. J. **C31**, 73 (2003), `arXiv:hep-ph/0306169`.

[52] S. P. Baranov, A. V. Lipatov, and N. P. Zotov, Phys. Rev. **D77**, 074024 (2008), `arXiv:0708.3560 [hep-ph]`.

[53] A. Kulesza and W. J. Stirling, Nucl. Phys. **B555**, 279 (1999), `arXiv:hep-ph/9902234`.

[54] D0 Collaboration, B. Abbott *et al.*, Phys. Rev. **D61**, 032004 (2000), `arXiv:hep-ex/9907009`.

[55] D0 Collaboration, B. Abbott *et al.*, Phys. Lett. **B513**, 292 (2001), `arXiv:hep-ex/0010026`.

[56] CDF Collaboration, A. A. Affolder *et al.*, Phys. Rev. Lett. **84**, 845 (2000), `arXiv:hep-ex/0001021`.

[57] G. Watt, A. D. Martin, and M. G. Ryskin, Phys. Rev. **D70**, 014012 (2004), `arXiv:hep-ph/0309096`.

[58] J. M. Campbell, R. K. Ellis, and D. L. Rainwater, Phys. Rev. **D68**, 094021 (2003),
`arXiv:hep-ph/0308195`;
J. M. Campbell and R. K. Ellis, Phys. Rev. **D65**, 113007 (2002),
`arXiv:hep-ph/0202176`;
J. Campbell and K. Ellis `http://mcfm.fnal.gov/`.

[59] J. Pumplin, D. Stump, J. Huston, H. Lai, P. Nadolsky, and W. Tung, JHEP
0207, 012 (2002). `http://www.citebase.org/abstract?id=oai:`
`arXiv.org:hep-ph/0201195`.

[60] S. P. Baranov and N. P. Zotov, Phys. Lett. **B491**, 111 (2000).

[61] J. Bartels, A. Sabio Vera, and F. Schwennsen, JHEP **0611**, 051 (2006),
`hep-ph/0608154`.

[62] J. Bartels, S. Gieseke, and C. F. Qiao, Phys. Rev. **D63**, 056014 (2001),
`arXiv:hep-ph/0009102`.

[63] J. Bartels, S. Gieseke, and A. Kyrieleis, Phys. Rev. **D65**, 014006 (2002),
`arXiv:hep-ph/0107152`.

[64] J. Bartels, D. Colferai, S. Gieseke, and A. Kyrieleis, Phys. Rev. **D66**, 094017 (2002),
`arXiv:hep-ph/0208130`.

[65] J. Bartels and A. Kyrieleis, Phys. Rev. **D70**, 114003 (2004),
`arXiv:hep-ph/0407051`.

[66] G. Chachamis and J. Bartels, PoS **DIFF2006**, 026 (2006).

[67] V. S. Fadin and L. N. Lipatov, Phys. Lett. **B429**, 127 (1998),
`arXiv:hep-ph/9802290`.

[68] M. Ciafaloni and G. Camici, Phys. Lett. **B430**, 349 (1998),
`arXiv:hep-ph/9803389`.

[69] V. S. Fadin (1998), `arXiv:hep-ph/9807528`.

[70] A. Sabio Vera, Nucl. Phys. **B746**, 1 (2006), `arXiv:hep-ph/0602250`.

[71] A. Sabio Vera and F. Schwennsen, Nucl. Phys. **B776**, 170 (2007),
`arXiv:hep-ph/0702158`.

[72] F. Schwennsen (2007), `arXiv:hep-ph/0703198`.

[73] A. Sabio Vera and F. Schwennsen, Phys. Rev. **D77**, 014001 (2008),
`arXiv:0708.0549 [hep-ph]`.

[74] A. H. Mueller and H. Navelet, Nucl. Phys. **B282**, 727 (1987).

[75] C. Marquet and C. Royon, Nucl. Phys. **B739**, 131 (2006), `arXiv:hep-ph/0510266`.

[76] O. Kepka, C. Royon, C. Marquet, and R. B. Peschanski, Phys. Lett. **B655**, 236 (2007), `arXiv:hep-ph/0609299`.

[77] O. Kepka, C. Royon, C. Marquet, and R. B. Peschanski, Eur. Phys. J. **C55**, 259 (2008), `arXiv:hep-ph/0612261`.

[78] C. Marquet and C. Royon (2007), `arXiv:0704.3409 [hep-ph]`.

[79] J. Bartels, D. Colferai, and G. P. Vacca, Eur. Phys. J. **C24**, 83 (2002), `arXiv:hep-ph/0112283`.

[80] J. Bartels, D. Colferai, and G. P. Vacca, Eur. Phys. J. **C29**, 235 (2003), `arXiv:hep-ph/0206290`.

[81] A. V. Kotikov and L. N. Lipatov, Nucl. Phys. **B582**, 19 (2000), `arXiv:hep-ph/0004008`.

[82] G. P. Salam, JHEP **07**, 019 (1998), `arXiv:hep-ph/9806482`.

[83] M. Ciafaloni, D. Colferai, G. P. Salam, and A. M. Stasto, Phys. Rev. **D68**, 114003 (2003), `arXiv:hep-ph/0307188`.

[84] A. Sabio Vera, Nucl. Phys. **B722**, 65 (2005), `arXiv:hep-ph/0505128`.

[85] D0 Collaboration, S. Abachi *et al.*, Phys. Rev. Lett. **77**, 595 (1996), `arXiv:hep-ex/9603010`.

[86] V. Del Duca and C. R. Schmidt, Phys. Rev. **D49**, 4510 (1994), `arXiv:hep-ph/9311290`.

[87] W. J. Stirling, Nucl. Phys. **B423**, 56 (1994), `arXiv:hep-ph/9401266`.

[88] J. Bartels, V. Del Duca, and M. Wusthoff, Z. Phys. **C76**, 75 (1997), `arXiv:hep-ph/9610450`.

[89] P. Aurenche, R. Basu, and M. Fontannaz (2008), `arXiv:0807.2133 [hep-ph]`.

[90] B. L. Combridge and C. J. Maxwell, Nucl. Phys. **B239**, 429 (1984).

[91] L. N. Lipatov, Sov. J. Nucl. Phys. **23**, 338 (1976).

[92] E. A. Kuraev, L. N. Lipatov, and V. S. Fadin, Sov. Phys. JETP **45**, 199 (1977).

[93] I. I. Balitsky and L. N. Lipatov, Sov. J. Nucl. Phys. **28**, 822 (1978).

[94] J. G. Contreras, R. B. Peschanski, and C. Royon, Phys. Rev. **D62**, 034006 (2000), `arXiv:hep-ph/0002057`.

[95] C. Marquet, R. B. Peschanski, and C. Royon, Phys. Lett. **B599**, 236 (2004), `arXiv:hep-ph/0407011`.

[96] M. Ciafaloni, Phys. Lett. **B429**, 363 (1998), `arXiv:hep-ph/9801322`.

[97] H1 Collaboration, A. Aktas *et al.*, Eur. Phys. J. **C46**, 27 (2006), `arXiv:hep-ex/0508055`.

[98] C. D. White, R. B. Peschanski, and R. S. Thorne, Phys. Lett. **B639**, 652 (2006), `arXiv:hep-ph/0606169`.

[99] X. e. a. Aslanoglou, Eur. Phys. J. **C52**, 495 (2007), `arXiv:0706.2641 [physics.ins-det]`.

[100] L. Lonnblad, Comput. Phys. Commun. **71**, 15 (1992).

[101] ZEUS Collaboration, S. e. a. Chekanov, Phys. Lett. **B632**, 13 (2006), `arXiv:hep-ex/0502029`.

[102] X. Aslanoglou, A. Cyz, N. Davis, D. d'Enterria, E. Gladysz-Dziadus, C. Kalfas, Y. Musienko, A. Kuznetsov, and A. D. Panagiotou (2007), `arXiv:0706.2576 [physics.ins-det]`.